

GEOMETRIC GENERALIZATION OF NEURAL OPERATORS FROM KERNEL INTEGRAL PERSPECTIVE*

MINGYU HAN[†], DANIEL ZHENGYU HUANG[‡], YUHAN WANG[†], YANSHU ZHANG[†],
AND JIAYI ZHOU[†]

Abstract. Neural operators are neural network-based surrogate models for approximating solution operators of parametric partial differential equations, enabling efficient many-query computations in science and engineering. Many applications, including engineering design, involve variable and often nonparametric geometries, for which generalization to unseen geometries remains a central practical challenge. In this work, we adopt a kernel integral perspective motivated by classical boundary integral formulations and recast operator learning on variable geometries as the approximation of geometry-dependent kernel operators, potentially with singularities. This perspective clarifies a mechanism for geometric generalization and reveals a direct connection between operator learning and fast kernel summation methods. Leveraging this connection, we propose a multiscale neural operator inspired by Ewald summation for learning and efficiently evaluating unknown kernel integrals, and we provide theoretical accuracy guarantees for the resulting approximation. Numerical experiments demonstrate robust generalization across diverse geometries for several commonly used kernels and for a large-scale three-dimensional fluid dynamics example.

Key words. Parametric partial differential equations, Surrogate modeling, Neural networks, Boundary integral methods, Singular kernels

AMS subject classifications. 65N38, 68T07, 65N80

1. Introduction. This paper develops neural network-based surrogate models for parametric partial differential equations (PDEs) defined on variable geometries. Such surrogates are valuable in settings that require rapid repeated PDE evaluations across changing domains. Representative applications include engineering design [1, 67, 42, 54, 65], where fast screening of candidate geometries is essential, and biomedical applications [22, 77, 80, 27], where a single model is expected to generalize across patient-specific anatomies (e.g., blood flow and tissue deformation).

We consider an abstract parametric PDE defined on a domain $\Omega \subset \mathbb{R}^d$

$$(1.1) \quad \mathcal{R}(u, a) = 0,$$

where \mathcal{R} denotes a generalized differential operator, $a : \mathbb{R}^d \rightarrow \mathbb{R}^{d_a}$ represents the parameter function, and $u(x) : \mathbb{R}^d \rightarrow \mathbb{R}^{d_u}$ represents the solution function. Solving (1.1) gives the solution operator

$$(1.2) \quad \mathcal{G}^\dagger : (a, \mathcal{D}) \mapsto u,$$

where \mathcal{D} denotes the geometry—either the domain Ω itself or, when only boundary quantities of interest are considered (e.g., aerodynamic loads on a vehicle), the boundary $\partial\Omega$. The goal of surrogate modeling is to learn \mathcal{G}^\dagger from data $\{a_i, \mathcal{D}_i, u_i = \mathcal{G}^\dagger(a_i, \mathcal{D}_i)\}_{i=1}^n$, especially when the geometry \mathcal{D} is nonparametric and may vary substantially across instances, potentially including topological changes.

*Submitted to the editors DATE. The authors are in alphabetical order.

Funding: We acknowledge funding support from National Key R&D Program of China 2025YFA1018700, National Natural Science Foundation of China (No.62595771, 12471403, and 12288101), and the Fundamental Research Funds for the Central Universities of China.

[†]School of Mathematical Sciences, Peking University, Beijing, China (hanmy2023@stu.pku.edu.cn, wyhan@stu.pku.edu.cn, yanshu@stu.pku.edu.cn, jiayi22@stu.pku.edu.cn).

[‡]Corresponding author. Beijing International Center for Mathematical Research, Center for Machine Learning Research, Peking University, Beijing, China (huangdz@bicmr.pku.edu.cn).

To motivate our approach, consider Laplace's equation on a bounded domain Ω with smooth boundary $\partial\Omega$:

$$(1.3) \quad \begin{aligned} \Delta u &= 0 && \text{in } \Omega, \\ u(x) &= f(x) && \text{on } \partial\Omega. \end{aligned}$$

Let $\kappa(x)$ denote the fundamental solution satisfying $-\Delta_x \kappa(x) = \delta_0(x)$. Classical panel methods [32] and boundary element methods [63][69, Chapter 7] represent solutions via layer potentials. In particular, the double layer potential yields the representation

$$(1.4) \quad u(x) = \int_{\partial\Omega} \sigma(y) \frac{\partial_y \kappa(x-y)}{\partial n_y} dy \quad x \in \partial\Omega,$$

where σ is an unknown density on $\partial\Omega$ and n_y denotes the outward unit normal at $y \in \partial\Omega$. To determine σ , we enforce the boundary condition by taking the non-tangential limit of (1.4) as $x \rightarrow \partial\Omega$. Because the double layer kernel is weakly singular, the potential exhibits a jump discontinuity across $\partial\Omega$, and the limit taken from within Ω satisfies the classical jump relation

$$(1.5) \quad f(x) = -\frac{1}{2}\sigma(x) + \text{p.v.} \int_{\partial\Omega} \sigma(y) \frac{\partial_y \kappa(x-y)}{\partial n_y} dy \quad x \in \partial\Omega,$$

where p.v. denotes the Cauchy principal value. Equation (1.5) is a Fredholm integral equation of the second kind for σ . Once σ is obtained, the solution u can be evaluated throughout Ω using (1.4). Consequently, the composition of (1.5) and (1.4) defines the solution operator for (1.3).

From this perspective, learning the solution operator (1.2) on variable geometries can be viewed as learning a geometry-dependent and potentially singular kernel κ , together with its associated operations: kernel integration, the solution of Fredholm integral equations, and their compositions. Since a Fredholm integral equation of the second kind admits a Neumann series expansion [41, Section 2.4] in terms of repeated kernel integration, accurately learning the kernel integral operator is the central task. Motivated by this view, we represent geometries \mathcal{D} as point clouds [60, 43, 79] and design kernel-based neural operators that act directly on functions defined over \mathcal{D} . The proposed neural operator is built by composing parameterized kernel integral operators on \mathcal{D} (i.e., (1.4) and (1.5)), implemented with efficient evaluation, with pointwise nonlinearities, thereby approximating the solution operator without requiring an explicit geometric parameterization. This formulation naturally promotes generalization across diverse geometries, including settings with significant geometric and topological variation.

1.1. Contributions. We adopt a kernel integral perspective on neural operators to better understand and improve their ability to generalize across variable geometries. Specifically, our contributions include:

1. We study the universal approximation of singular kernel integrals via a multi-scale decomposition inspired by Ewald summation, and we derive corresponding error bounds.
2. We introduce the Multiscale Point Cloud Neural Operator (M-PCNO), a neural network-based surrogate for PDEs on variable geometries with linear computational cost in the number of points. Its layer design is guided by the multiscale kernel approximation developed above. We also release an educational software package at <https://github.com/PKU-CMEGroup/NeuralOperator>.

3. We demonstrate geometric generalization in representative numerical experiments across diverse geometries, including a large-scale three-dimensional fluid dynamics example.

1.2. Preliminaries and Literature Review. This work aims to advance the understanding of how neural operators generalize when learning PDE solution operators on variable geometries. In this section, we review related neural operator approaches and classical fast kernel summation methods. The latter provides guiding principles for constructing linear operators that approximate singular kernel integrals efficiently.

1.2.1. Neural Operator Approaches. Neural operators [81, 37, 53, 45] are neural network-based surrogate models that approximate PDE solution operators such as (1.2). Their key feature is that they approximate mappings between function spaces at the continuous level, rather than solutions at a fixed discretization. By separating the operator representation from the discretization used in computation, neural operators can generalize across mesh resolutions. Existing architectures are typically built from integral operators [45, 40, 23, 8, 10], often motivated by Green’s functions, or from differential operators [52, 79]; in either case, a standard numerical discretization is applied afterward to obtain concrete algorithms.

Extending neural operators to variable computational domains remains challenging. Common strategies either map each geometry to a fixed reference domain via a parametric deformation [44, 77, 75], or embed the domain into a fixed bounding box, for example, using zero padding or signed distance functions [29, 76, 15, 50, 48]. Both approaches reduce the problem to a fixed representation and enable the use of standard neural operator architectures. However, deformation maps may not be well-defined for complex geometries [75], and embedding-based approaches often rely on mesh-resolution-dependent interpolation or extrapolation.

An alternative strategy represents variable geometries \mathcal{D} as point clouds, which naturally encode detailed geometric information. Point cloud networks, such as PointNet [60] and its extensions [61, 43], enable the extraction of geometric features for tasks such as classification and segmentation. Operator learning frameworks, including DeepONet [53, 34] and transformer-based models [11, 36, 74, 73, 72], have also been extended to operate on point cloud representations, often using encoder-based architectures to reduce memory and computational costs. When connectivity information among points is available, graph neural networks provide a natural framework for PDE surrogate modeling [58, 51, 21, 66]. Although standard graph-based methods can be sensitive to mesh resolution, mesh-independent aggregation can mitigate this dependence, leading to graph neural operators [46, 47, 56]. Moreover, point cloud representations can be augmented with additional geometric information to further improve accuracy and robustness [24, 29, 76, 15, 64, 62]. In this work, we adopt the point cloud strategy and design neural operators that act directly on geometries \mathcal{D} represented as point clouds. Guided by boundary element formulations such as (1.4) and (1.5), we study how these operators generalize under variations in domain geometry.

1.2.2. Classical Fast Kernel Summation Methods. Neural operators are often built from kernel integral operators, motivated by Green’s functions. In many PDE settings, the associated kernels are singular and depend explicitly on geometric quantities such as boundary normals. Moreover, efficient evaluation of these kernel integrals is crucial for deployment at scale. These issues have received comparatively

less attention in the neural operator literature, but they are central to the present work. We therefore review classical fast kernel summation methods for efficiently evaluating singular kernel integrals, which motivate our neural operator design.

Methods such as the fast multipole method [3, 25, 2, 12, 78, 20] and hierarchical matrix techniques [28, 4, 6] accelerate dense kernel matrix–vector multiplications by exploiting scale separation: far-field interactions are approximated using low-rank representations, while near-field interactions involving potentially singular kernels are evaluated exactly. As a result, these methods can achieve linear or quasi-linear computational complexity. Several works have explored neural operators inspired by such multiscale ideas [18, 19, 7, 71]. However, incorporating these fast summation methods into learning-based neural operators for general kernels, especially in a manner optimized for modern GPU architectures, remains challenging. In this work, we revisit an earlier strategy originating with Ewald summation [17, 13, 33], in which far-field interactions are approximated in the Fourier domain [5, 59, 70], while local interactions are computed exactly or approximated via local Taylor expansions [26]. We adopt this strategy to the design of neural operators and demonstrate its effectiveness across a broad class of kernels and related problems, achieving moderate accuracy while naturally enabling efficient GPU implementations.

1.3. Organization. In [section 2](#), we study Ewald–type decompositions for approximating singular kernels and provide a theoretical analysis of the resulting approximation errors. Building on these results, [section 3](#) develops neural layers for efficient kernel integration across a broad class of commonly encountered kernels. [Section 4](#) introduces the M-PCNO. Numerical experiments in [section 5](#) validate the theory and demonstrate geometric generalization. Finally, [section 6](#) provides concluding remarks.

2. Approximation of Singular Kernels. In this section, we consider variable geometries Ω and assume that each geometry is contained in the box

$$B = [0, l_1] \times [0, l_2] \times \cdots \times [0, l_d],$$

where d is the spatial dimension and $\{l_i\}$ are the side lengths in each coordinate direction. We further assume a uniform separation from the boundary: there exists $d_B > 0$ such that $\text{dist}(\Omega, \partial B) \geq d_B$ for all geometries under consideration. Many physical problems of practical interest in this setting involve layer potentials:

$$(2.1a) \quad \text{Single layer potential : } Sf(x) = \int_{\partial\Omega} \kappa(x - y) f(y) dy,$$

$$(2.1b) \quad \text{Double layer potential : } Df(x) = \int_{\partial\Omega} \frac{\partial \kappa(x - y)}{\partial n_y} f(y) dy,$$

$$(2.1c) \quad \text{Adjoint double layer potential : } D^*f(x) = \int_{\partial\Omega} \frac{\partial \kappa(x - y)}{\partial n_x} f(y) dy,$$

and the volume potential:

$$(2.2) \quad Vf(x) = \int_{\Omega} \kappa(x - y) f(y) dy.$$

Here κ is a translation-invariant kernel. A canonical example is the fundamental solution of the Laplace:

$$(2.3) \quad \kappa(x - y) = \begin{cases} -\frac{1}{2\pi} \ln \|x - y\|_2 & d = 2 \\ \frac{1}{d(d-2)\alpha_d \|x - y\|_2^{d-2}} & d > 2, \end{cases}$$

where α_d denotes the surface area of the unit sphere in \mathbb{R}^d .

A central objective of this work is to learn κ and efficiently evaluate the integrals in (2.1) and (2.2). Since $\Omega \subset B$, all differences $x - y$ lie in

$$(2.4) \quad B_2 = [-l_1, l_1] \times [-l_2, l_2] \times \cdots \times [-l_d, l_d].$$

Accordingly, we focus on learning $\kappa : B_2 \rightarrow \mathbb{R}$. We further assume that κ is periodic on B_2 . When the original kernel is not periodic, Fourier continuation [9] can be used to construct a smooth periodic extension on B_2 . This is justified because the geometries of interest remain at least a distance d_B away from the boundary, so the periodic extension does not affect kernel evaluations on the geometries considered.

Because the kernel κ is generally singular at the origin, efficient evaluation of the integrals in (2.1) and (2.2) typically requires multiscale strategies that separate long- and short-range interactions. For example, for the three-dimensional Coulomb kernel $\kappa(x - y) = \frac{1}{r}$ with $r = \|x - y\|_2$, Ewald summation [17] employs the decomposition

$$(2.5) \quad \frac{1}{r} = \frac{\text{erf}(r/\delta)}{r} + \frac{\text{erfc}(r/\delta)}{r}, \quad \text{where } \text{erf}(r) = \frac{2}{\sqrt{\pi}} \int_0^r e^{-t^2} dt, \quad \text{erfc}(r) = 1 - \text{erf}(r).$$

Here $\delta > 0$ is the Ewald splitting parameter that separates the long- and short-range contributions. The first term is a smooth long-range component (including at $r = 0$) and can be handled efficiently in Fourier space. The second term is a localized short-range component that decays rapidly for $r \gtrsim \delta$

$$\frac{\text{erfc}(r/\delta)}{r} = \frac{2}{r\sqrt{\pi}} \int_{r/\delta}^{\infty} e^{-t^2} dt \leq \frac{2}{r\sqrt{\pi}} \int_{r/\delta}^{\infty} e^{-t^2} \frac{t}{r/\delta} dt = \frac{\delta}{\sqrt{\pi}r^2} e^{-r^2/\delta^2}.$$

Consequently, the short-range contribution can be evaluated directly (or with local approximations) on a neighborhood of size $\mathcal{O}(\delta)$.

Motivated by the Ewald splitting (2.5), we introduce an Ewald-type decomposition for general singular kernels. This decomposition supports efficient evaluation and yields polynomially decaying approximation error bounds, summarized in the following theorem. The proof is deferred to section A.

THEOREM 2.1. *Let κ be a periodic, translation-invariant kernel on $B_2 = [-\frac{1}{2}, \frac{1}{2}]^d$ with $d \geq 2$. Assume that $\kappa(x) \in L^1(B_2) \cap C^2(B_2 \setminus \{0\})$ and that there exists a constant $C > 0$ such that*

$$(2.6) \quad \|\nabla^k \kappa(x)\|_2 \leq \frac{C}{\|x\|_2^{k+d-1}} \quad k = 0, 1, 2,$$

for all $x \in B_2 \setminus \{0\}$. For $\delta \in (0, \frac{1}{2})$, define the Gaussian mollifier $\rho_\delta(y) = \frac{1}{(2\pi\delta^2)^{d/2}} e^{-\frac{\|y\|_2^2}{2\delta^2}}$ and decompose

$$(2.7) \quad \kappa(x) = \kappa_{\text{long}}(x) + \kappa_{\text{short}}(x), \quad \kappa_{\text{long}} := \kappa * \rho_\delta, \quad \kappa_{\text{short}} := \kappa - \kappa * \rho_\delta,$$

where $*$ denotes convolution. Then the following estimates hold:

1. For the long-range component, let $\widehat{\kappa}_{\text{long}}_k$ denote the Fourier coefficients of κ_{long} on B_2 (with integer multi-index k). Truncating the Fourier series to $\|k\|_\infty \leq p$ yields the uniform bound:

$$(2.8) \quad \left\| \kappa_{\text{long}}(x) - \sum_{\|k\|_\infty \leq p} \widehat{\kappa}_{\text{long}}_k e^{2\pi i k \cdot x} \right\|_{L^\infty(B_2)} \leq C_{\text{long}}(d, \kappa) \frac{e^{-2\pi^2 \delta^2 p^2}}{\delta^{d+1} p},$$

where $C_{\text{long}}(d, \kappa) = \frac{d\|\kappa\|_{L^1(B_2)}}{2\pi^2}(1 + \frac{1}{\sqrt{2\pi}})^{d-1}$.

2. For the short-range component, the kernel is localized. For any $\alpha \in (0, \frac{2}{d+1})$, and any x satisfying $\|x\|_2 \geq \delta$, we have

$$(2.9) \quad \left| \kappa_{\text{short}}(x) \right| \leq \frac{dC\delta^{2-\alpha(d+1)}}{2\|x\|_2^{d+1}} + C_{\text{short}}(d, \alpha, \kappa) \frac{e^{-\frac{1}{2}(1-\delta^\alpha)^2 \frac{\|x\|_2^2}{\delta^2}}}{\delta^d},$$

where

$$C_{\text{short}}(d, \alpha, \kappa) = \frac{\|\kappa\|_{L^1(B_2)}}{(2\pi)^{d/2}} \left(1 + \frac{2^d d}{(1 - e^{-1/2})^d} \right) + \frac{CC_{d/2}}{\Gamma(\frac{d}{2})} \left(\frac{1}{2^{d/2}} + \frac{1}{(1 - 2^{-\alpha})^2} \right).$$

Here Γ denotes the Gamma function, and $C_{d/2}$ is the Gamma-function-related constant defined in [Lemma A.1](#).

3. Assume that κ_{short} admits a local approximation on the Euclidean ball $B_\epsilon = \{x : \|x\|_2 \leq \epsilon\}$ by a function $\tilde{\kappa}_{\text{short}}$, with accuracy $\mathcal{O}(\epsilon^{d+q})$, in the sense that

$$(2.10) \quad \|\tilde{\kappa}_{\text{short}} - \kappa_{\text{short}}\|_{L^1(B_\epsilon)} \leq M\epsilon^{d+q},$$

for some local approximation order $q > 0$ and constant $M > 0$. Define

$$(2.11) \quad \tilde{\kappa}(x) = \sum_{\|k\|_\infty \leq p} \widehat{\kappa_{\text{long}}}_k e^{2\pi i k \cdot x} + \tilde{\kappa}_{\text{short}} \cdot \mathbb{1}_{B_\epsilon}(x).$$

Choose $\delta = p^{-\gamma}$, $\epsilon = \delta^t = p^{-\gamma t}$, and $t = \frac{2-\alpha(d+1)}{q+2d+1}$ with arbitrary parameters

$$(2.12) \quad \gamma \in (0, 1), \quad \alpha \in (0, \frac{2}{d+1}), \quad \text{and} \quad p > 2^{\frac{1}{\gamma}}.$$

Under these choices, we obtain the L^1 error bound

$$(2.13) \quad \begin{aligned} \|\tilde{\kappa} - \kappa\|_{L^1(B_2)} &\leq C_{\text{long}}(d, \kappa) p^{-1+\gamma(d+1)} e^{-2\pi^2 p^{2-2\gamma}} + \left(\frac{dC}{2} + M \right) p^{-\gamma t(q+d)} \\ &\quad + C_{\text{short}}(d, \alpha, \kappa) p^{d\gamma} e^{-\frac{1}{2}(1-\delta^\alpha)^2 p^{\gamma(2-2t)}} \\ &= \mathcal{O} \left(e^{-2\pi^2 p^{2-2\gamma}} + e^{-\frac{1}{2}(1-\delta^\alpha)^2 p^{\gamma(2-2t)}} + p^{-\gamma t(q+d)} \right). \end{aligned}$$

Remark 2.2. [Equation \(2.11\)](#) approximates the singular kernel κ by combining a truncated Fourier representation of the smooth long-range component with a localized approximation of the short-range component. The error bound [\(2.13\)](#) consists of two exponentially decaying terms and one polynomially decaying term. For sufficiently

large p , the polynomial term $p^{-\gamma t(q+d)} = p^{-\gamma \left(1 + \frac{q-1-\alpha(d+1)(q+d)}{q+2d+1} \right)}$ dominates. Since $\alpha \in (0, \frac{2}{d+1})$ and $\gamma \in (0, 1)$ in [\(2.12\)](#) are free parameters, we may take $\alpha \rightarrow 0, \gamma \rightarrow 1$, in

which case the polynomial decay rate approaches $p^{-\left(1 + \frac{q-1}{q+2d+1} \right)}$. This rate is strictly faster than $\mathcal{O}(p^{-1})$ when the local approximation order satisfies $q > 1$, and it can be made arbitrarily close to $\mathcal{O}(p^{-1})$ when $q = 1$. The theorem thus clarifies how the truncated mode number p (i.e., retaining modes with $\|k\|_\infty \leq p$) controls the approximation error, a relationship that is also observed numerically in [section 5](#).

Remark 2.3. The regularity assumptions on κ and its derivatives are satisfied by many commonly used kernels, including those listed in [Table 1](#); the verification is deferred to [subsection B.1](#). For simplicity, the theorem is stated on $B_2 = [-\frac{1}{2}, \frac{1}{2}]^d$; the corresponding estimates for a general box $B_2 = \Pi_{i=1}^d [-l_i, l_i]^d$ follow by rescaling. In the neural operator design below, we allow arbitrary bounding boxes.

Remark 2.4. This decomposition—combining a truncated Fourier representation with a localized approximation—serves as a useful conceptual template for our neural layer design. In classical Ewald-type decompositions, selecting the splitting parameter δ is not straightforward. In contrast, our neural layers explicitly include Fourier and local components and learn how to weight and combine them from data, without committing to the specific construction [\(2.11\)](#). [Theorem 2.1](#) can therefore be viewed as an achievability benchmark: it shows that this multiscale ansatz can attain an error no larger than [\(2.13\)](#) when training is effective.

3. Neural Layers for Kernel Integrals. In this section, we design neural layers that approximate singular kernel integrals with linear computational cost, guided by the Ewald-type decomposition in [Theorem 2.1](#). Specifically, we approximate the smooth long-range component using a truncated Fourier representation and treat the short-range component via localized Taylor expansions.

We consider kernel integrals defined either on the domain Ω or on its boundary $\partial\Omega$, and denote either case by $\mathcal{D} \subset \mathbb{R}^d$. Let \mathcal{K} be an integral operator acting on smooth \mathbb{R}^{d_f} -valued functions on \mathcal{D} ,

$$(3.1) \quad \mathcal{K} : \{f : \mathcal{D} \rightarrow \mathbb{R}^{d_f}\} \longrightarrow \{f : \mathcal{D} \rightarrow \mathbb{R}^{d_f}\},$$

defined by

$$(3.2) \quad (\mathcal{K}f)(x) = \int_{\mathcal{D}} \kappa(x - y; n_x, n_y) f(y) dy, \quad x \in \mathcal{D}.$$

Here κ is translation-invariant in the displacement $x - y$ and has a singularity at the origin. For boundary integrals ($\mathcal{D} = \partial\Omega$), the kernel may also depend on the outward unit normals n_x and n_y ; in the cases we consider, this dependence enters multiplicatively, which covers the kernels listed in [Table 1](#).

We first describe the approximation of the smooth long-range component and then the treatment of the localized short-range component. We then combine these ingredients to construct the proposed multiscale point cloud neural layer.

3.1. Long-Range Approximation. For the long-range component, we approximate the smooth part of the kernel-induced map in [\(3.2\)](#) by a truncated Fourier representation:

$$(3.3) \quad \int_{\mathcal{D}} \kappa_{\text{long}}(x - y; n_x, n_y) f(y) dy \approx \mathbb{K}_{\text{long}} f(x).$$

Specifically, we define

$$(3.4) \quad \mathbb{K}_{\text{long}} f(x) := \begin{cases} \sum_{\|k\|_{\infty} \leq p} \int_{\Omega} e^{2\pi i k \cdot \frac{x-y}{2l}} W_{v,1}^k f(y) dy & \mathcal{D} = \Omega \\ \sum_{\|k\|_{\infty} \leq p} \int_{\partial\Omega} e^{2\pi i k \cdot \frac{x-y}{2l}} \left(W_{v,1}^k f(y) + W_{v,2}^k (f(y) \otimes n_y) + W_{v,3}^k (f(y) \otimes n_x) \right) dy & \mathcal{D} = \partial\Omega, \end{cases}$$

with learnable matrices $W_{v,i}^k$ that parameterize different kernel components. We truncate the Fourier basis at $\|k\|_\infty \leq p$ and use the normalized coordinate

$$(3.5) \quad \frac{x-y}{2l} := \left(\frac{x_1-y_1}{2l_1}, \dots, \frac{x_d-y_d}{2l_d} \right),$$

where $\{l_i\}_{i=1}^d$ are determined by the bounding box B_2 in (2.4).

The term $W_{v,1}^k \in \mathbb{R}^{d_f \times d_f}$ captures kernels without explicit normal dependence, such as the single layer and volume potentials,

$$(3.6) \quad Sf(x) = \int_{\partial\Omega} \kappa(x-y) f(y) dy \quad Vf(x) = \int_{\Omega} \kappa(x-y) f(y) dy,$$

In this case, we approximate κ by a truncated Fourier series,

$$\kappa(x-y) \approx \sum_{\|k\|_\infty \leq p} e^{2\pi i k \cdot \frac{x-y}{2l}} W_{v,1}^k,$$

so that the integral reduces to a Fourier-feature convolution. This construction is closely related to Fourier layers [57, 45, 40, 35, 14], with the key distinction that the integrals are evaluated on the point cloud $\{x^{(i)}\}_{i=1}^N$ using numerical quadrature rather than fast Fourier transforms [49, 79].

For boundary operators ($\mathcal{D} = \partial\Omega$), kernels may depend on geometric quantities such as outward unit normals. The term $W_{v,2}^k \in \mathbb{R}^{d_f \times (d_f d)}$ captures dependence on n_y , as in the double layer potential,

$$(3.7) \quad Df(x) = \int_{\partial\Omega} \nabla_y \kappa(x-y) \cdot n_y f(y) dy.$$

In (3.4), the tensor product $f(y) \otimes n_y$ is reshaped into a vector of dimension $d_f d$, encoding the normal information at y . Similarly, $W_{v,3}^k \in \mathbb{R}^{d_f \times (d_f d)}$ captures dependence on n_x , as in the adjoint double layer potential,

$$(3.8) \quad D^*f(x) = \int_{\partial\Omega} \nabla_x \kappa(x-y) \cdot n_x f(y) dy.$$

In practice, when d_f is large, the matrices $W_{v,i}^k$ can be partially shared across $i = 1, 2, 3$ to reduce the number of kernel integral evaluations to improve computational efficiency. Specifically, we employ the factorized form

$$(3.9) \quad \begin{aligned} \mathbb{K}_{\text{long}}^{(1)} f(x) &:= \sum_k \int_{\partial\Omega} e^{2\pi i k \cdot \frac{x-y}{2l}} W_{v,1}^k W_1 \begin{bmatrix} f(y) \\ f(y) \otimes n_y \end{bmatrix} dy, \\ \mathbb{K}_{\text{long}} f(x) &:= W_3 \mathbb{K}_{\text{long}}^{(1)} f(x) + W_2 \begin{bmatrix} \mathbb{K}_{\text{long}}^{(1)} f(x) \\ \mathbb{K}_{\text{long}}^{(1)} f(x) \otimes n_x \end{bmatrix}, \end{aligned}$$

where $W_1, W_2 \in \mathbb{R}^{d_f \times d_f(d+1)}$ and $W_3 \in \mathbb{R}^{d_f \times d_f}$.

3.2. Short-Range Approximation. The short-range component targets the near-field portion of the kernel integral that is not well captured by the truncated Fourier representation (3.4), due to the kernel's singularity. Specifically, we approximate the contribution from the Euclidean ball $B_\epsilon(x) = \{y : \|y-x\|_2 \leq \epsilon\}$ centered at x :

$$(3.10) \quad \int_{\mathcal{D} \cap B_\epsilon(x)} \kappa'(x-y, n_x, n_y) f(y) dy \approx \mathbb{K}_{\text{short}} f(x),$$

where κ' denotes the remainder (short-range) kernel after subtracting the long-range Fourier component. To approximate (3.10), we apply an intrinsic Taylor expansion of f about x . For a smooth function f ,

$$(3.11) \quad f(y) = f(x) + \nabla_{\mathcal{D}} f(x) \cdot v(y) + \mathcal{O}(\|v(y)\|_2^2),$$

where $v(y) := \log_x(y) \in T_x \mathcal{D}$ is the tangent space coordinate of y at x induced by the logarithmic map. Because $y \in \mathcal{D} \cap B_\epsilon(x)$, we have $\|v(y)\|_2 = \mathcal{O}(\epsilon)$ provided \mathcal{D} is regular and ϵ is sufficiently small. When $\mathcal{D} = \Omega$, the operator $\nabla_{\mathcal{D}}$ coincides with the conventional gradient. When $\mathcal{D} = \partial\Omega$ is a curve or surface, $\nabla_{\mathcal{D}}$ denotes the tangential (surface/curve) gradient, i.e., the ambient gradient projected onto the tangent space. Substituting (3.11) into (3.10) yields

$$(3.12) \quad \int_{\mathcal{D} \cap B_\epsilon(x)} \kappa'(x-y) f(y) dy = M_0(x) f(x) + M_1(x) \cdot \nabla_{\mathcal{D}} f(x) + \mathcal{R}(x),$$

where the geometric moments are defined by

$$M_0(x) = \int_{\mathcal{D} \cap B_\epsilon(x)} \kappa'(x-y; n_x, n_y) dy, \quad M_1(x) = \int_{\mathcal{D} \cap B_\epsilon(x)} \kappa'(x-y; n_x, n_y) v(y) dy.$$

The remainder term $\mathcal{R}(x)$ arises from integrating the Taylor remainder $\mathcal{O}(\|v(y)\|_2^2)$ against the kernel.

Potential	Kernel	Short-range asymptotic approximation
2D Laplacian single layer potential	$\frac{-1}{2\pi} \log \ x-y\ _2$	$-\frac{\epsilon \log \epsilon - \epsilon}{\pi} f(x) + o(\epsilon^2)$
2D Laplacian double layer potential	$\frac{(x-y) \cdot n_y}{2\pi \ x-y\ _2^2}$	$-\frac{\epsilon \text{tr}[\nabla_{\mathcal{D}} n_x]}{2\pi} f(x) + \mathcal{O}(\epsilon^3)$
2D Modified Laplacian double layer potential	$\frac{x-y}{2\pi \ x-y\ _2^2}$	$-\frac{\epsilon \text{tr}[\nabla_{\mathcal{D}} n_x] n_x}{2\pi} f(x) - \frac{\epsilon}{\pi} \nabla_{\mathcal{D}} f(x) + \mathcal{O}(\epsilon^3)$
2D Adjoint Laplacian double layer potential	$\frac{(y-x) \cdot n_x}{2\pi \ x-y\ _2^2}$	$-\frac{\epsilon \text{tr}[\nabla_{\mathcal{D}} n_x]}{2\pi} f(x) + \mathcal{O}(\epsilon^3)$
2D Stokeslet	$\frac{1}{4\pi} \left(-\log \ x-y\ _2 I_2 + \frac{(x-y)(x-y)^T}{\ x-y\ _2^2} \right)$	$-\frac{\epsilon \log \epsilon + \epsilon}{2\pi} f(x) + \frac{\epsilon}{2\pi} (I_2 - n_x n_x^T) f(x) + o(\epsilon^2)$
3D Laplacian single layer potential	$\frac{1}{4\pi \ x-y\ _2}$	$\frac{\epsilon}{2} f(x) + \mathcal{O}(\epsilon^3)$
3D Laplacian double layer potential	$\frac{(y-x) \cdot n_y}{4\pi \ x-y\ _2^3}$	$\frac{\epsilon \text{tr}[\nabla_{\mathcal{D}} n_x]}{8} f(x) + \mathcal{O}(\epsilon^3)$
3D Modified Laplacian double layer potential	$\frac{y-x}{4\pi \ x-y\ _2^3}$	$\frac{\epsilon \text{tr}[\nabla_{\mathcal{D}} n_x] n_x}{8} f(x) + \frac{\epsilon}{4} \nabla_{\mathcal{D}} f(x) + \mathcal{O}(\epsilon^3)$
3D Adjoint Laplacian double layer potential	$\frac{(x-y) \cdot n_x}{4\pi \ x-y\ _2^3}$	$\frac{\epsilon \text{tr}[\nabla_{\mathcal{D}} n_x]}{8} f(x) + \mathcal{O}(\epsilon^3)$
3D Stokeslet	$\frac{1}{8\pi} \left(\frac{1}{\ x-y\ _2} I_3 + \frac{(x-y)(x-y)^T}{\ x-y\ _2^2} \right)$	$\frac{\epsilon}{4} f(x) + \frac{\epsilon}{8} (I - n_x n_x^T) f(x) + \mathcal{O}(\epsilon^3)$

Table 1: Summary of common 2D and 3D layer potentials, their kernels, and short-range asymptotic approximations of $\int_{\partial\Omega \cap B_\epsilon(x)} \kappa'(x-y; n_x, n_y) f(y) dy$. The derivations are deferred to subsection B.2.

These geometric moments M_0 and M_1 encode both local geometry and the kernel profile. To illustrate their structure, we consider several commonly used 2D and 3D layer potentials; the resulting short-range asymptotic approximations of (3.12) are summarized in Table 1. In these examples, the leading-order behavior is captured by (3.12), and the remainder is high order in ϵ —at least one order beyond the intrinsic

dimension of \mathcal{D} . Moreover, for the kernels in [Table 1](#), the moments M_0 and M_1 can be expressed as low-order polynomials in the outward normal n_x and the curvature $\text{tr}[\nabla_{\mathcal{D}} n_x]$. Motivated by this structure, we define the following short-range operator to approximate [\(3.12\)](#):

$$(3.13) \quad \mathbb{K}_{\text{short}} f(x) := \begin{cases} W_l f(x) + b + W_{g,1} \nabla_{\mathcal{D}} f(x) & \mathcal{D} = \Omega \\ W_l f(x) + b + W_{g,1} \nabla_{\mathcal{D}} f(x) + W_{g,2} \left(W_{g,3} \begin{bmatrix} n_x \\ \nabla_{\mathcal{D}} n_x \end{bmatrix} \odot W_{g,4} f(x) \right) & \mathcal{D} = \partial\Omega, \end{cases}$$

where \odot denotes the elementwise product. The learnable matrices $W_l, W_{g,2}, W_{g,4} \in \mathbb{R}^{d_f \times d_f}$, $W_{g,1} \in \mathbb{R}^{d_f \times (d_f d)}$, and $W_{g,3} \in \mathbb{R}^{d_f \times (d^2 + d)}$ are designed to capture these geometric moments. Although [\(3.13\)](#) is only linear in n_x and $\nabla_{\mathcal{D}} n_x$, composing this operator in a multi-layer network enables accurate representation of the short-range asymptotic approximations in [Table 1](#). Higher-degree polynomial features of n_x and $\nabla_{\mathcal{D}} n_x$ can also be incorporated into [\(3.13\)](#) to improve accuracy with minimal computational overhead.

3.3. Multiscale Point Cloud Neural Layer. We now combine the long-range operator \mathbb{K}_{long} from [subsection 3.1](#) and the short-range operator $\mathbb{K}_{\text{short}}$ from [subsection 3.2](#) to form a multiscale point cloud neural layer \mathcal{L} . The layer has a residual (ResNet) architecture [\[30\]](#) and maps an input function $f : \mathcal{D} \rightarrow \mathbb{R}^{d_f}$ to an output function $\mathcal{L}f : \mathcal{D} \rightarrow \mathbb{R}^{d_f}$ via

$$(3.14) \quad \mathcal{L}f(x) = f(x) + \sigma \left(\mathbb{K}_{\text{long}} f(x) + \mathbb{K}_{\text{short}} f(x) \right).$$

where σ is a pointwise activation function; throughout, we use the Gaussian Error Linear Unit (GeLU) [\[31\]](#).

The split between long- and short-range contributions—including the effective cutoff scale ϵ in [\(3.10\)](#)—is not prescribed a priori, but is learned from data through the parameters of \mathbb{K}_{long} and $\mathbb{K}_{\text{short}}$. Moreover, while each layer employs translation-invariant kernels (in the displacement $x - y$), the target solution operator need not be translation-invariant—for example, operators arising from Fredholm integral equations such as [\(1.5\)](#). In such cases, the associated resolvent can be represented by a Neumann series involving repeated applications of a kernel integral operator. Network depth, therefore, plays a natural role in capturing this iterative structure, and deeper architectures can improve approximation accuracy.

4. Multiscale Point Cloud Neural Operator. In this section, we introduce the Multiscale Point Cloud Neural Operator (M-PCNO), to approximate the solution operator

$$(4.1) \quad \mathcal{G}^\dagger : (a, \mathcal{D}) \mapsto u,$$

where $a : \mathcal{D} \rightarrow \mathbb{R}^{d_a}$ and $u : \mathcal{D} \rightarrow \mathbb{R}^{d_u}$ are functions defined on \mathcal{D} . Our primary focus is on boundary setting $\mathcal{D} = \partial\Omega$, where quantities of interest, such as aerodynamic loads on a vehicle, are evaluated.

We augment the input with geometric features and define

$$(4.2) \quad \tilde{a} : \mathcal{D} \rightarrow \mathbb{R}^{d_a + 2d}, \quad \tilde{a}(x) = \begin{bmatrix} a(x) \\ x \\ n_x \end{bmatrix},$$

which concatenates the parameter function a with the identity embedding $x = \text{id}(x)$ and the normal field $n : \mathcal{D} \rightarrow \mathbb{R}^d, x \rightarrow n_x$, thereby encoding geometric information about \mathcal{D} . At the implementation level, the input $\tilde{\mathbf{a}} \in \mathbb{R}^{N \times (d_a + 2d)}$ consists of evaluations of \tilde{a} on a point cloud $X = \{x^{(i)}\}_{i=1}^N \subset \mathcal{D}$ with N points that discretizes the domain.

The first layer is a lifting layer implemented by a pointwise neural network:

$$(4.3) \quad f(x) = \sigma(W\tilde{a}(x) + b),$$

with $W \in \mathbb{R}^{d_f \times (d_a + 2d)}$ and $b \in \mathbb{R}^{d_f}$. This layer lifts the feature dimension from $d_a + 2d$ to a higher-dimensional space d_f , increasing expressivity and making subsequent operator learning more effective [39, 55].

Following the lifting layer, the network applies several multiscale point cloud neural layers (3.14). For the long-range operator \mathbb{K}_{long} in (3.4), the integrals are evaluated using numerical quadrature on the point cloud. For example,

$$(4.4) \quad \sum_{\|k\|_\infty \leq p} \int_{\mathcal{D}} e^{2\pi i k \cdot \frac{x-y}{2l}} W_{v,1}^k f(y) dy \approx \sum_{\|k\|_\infty \leq p} e^{2\pi i k \cdot \frac{x}{2l}} W_{v,1}^k \left(\sum_{i=1}^N e^{-2\pi i k \cdot \frac{y^{(i)}}{2l}} f(y^{(i)}) d\Omega^{(i)} \right),$$

where $d\Omega^{(i)}$ denotes the quadrature weight (e.g., the local mesh size) associated with the point $y^{(i)}$, precomputed from the point cloud/mesh. When the truncated mode number p is modest, the computational cost scales as $\mathcal{O}(p^d N)$, where N is the number of points and p^d is the number of retained Fourier modes. For the short-range operator $\mathbb{K}_{\text{short}}$ in (3.13), spatial gradients are approximated using a least-squares method [79, Section 3.2]. Specifically, the gradient $\nabla_{\mathcal{D}} f(x^{(i)})$ is estimated from the function values at $x^{(i)}$ and a local neighborhood of nearby points; a neighborhood size on the order of d typically suffices to make the local least-squares system well conditioned. Neighbor sets are precomputed from the point cloud or an associated connectivity graph. The gradient estimation can be implemented as a single message-passing step with overall cost $\mathcal{O}(dN)$. To mitigate large gradients caused by discontinuities or sharp features in f and in geometric field n_x , we replace $\nabla_{\mathcal{D}} f$ by a smoothed gradient obtained by applying the **SoftSign** function componentwise:

$$(4.5) \quad \tilde{\nabla}_{\mathcal{D}} f(x) = \text{SoftSign}(\nabla_{\mathcal{D}} f(x)) \quad \text{where} \quad \text{SoftSign}(x) = \frac{x}{1 + |x|}.$$

The smoothed gradient $\tilde{\nabla}_{\mathcal{D}} f$ preserves essential gradient information while providing a robust indicator of sharp local variations. We apply the same smoothing strategy to derivatives of the geometric feature n_x ; specifically, the corresponding term in (3.13) takes the form

$$\text{SoftSign}\left(W_{g,3} \begin{bmatrix} n_x \\ \nabla_{\mathcal{D}} n_x \end{bmatrix}\right).$$

Overall, the multiscale point cloud neural layers employ traditional numerical discretizations, using numerical quadrature for integration and least squares for gradient estimation. This allows the method to handle varying spatial resolutions, with discretization error controlled by local mesh size rather than by the learning procedure.

In the final projection layer, we project the hidden representation back to d_u output channels. In this work, the projection layer consists of two pointwise linear

layers with a nonlinearity:

$$(4.6) \quad u(x) = W' \sigma(W f(x) + b) + b',$$

where $W' \in \mathbb{R}^{d_u \times d_u}$ and $b' \in \mathbb{R}^{d_u}$.

We train the M-PCNO in a supervised setting using a dataset $\{a_i, \mathcal{D}_i, u_i\}_{i=1}^n$, where $\{u_i = \mathcal{G}^\dagger(a_i, \mathcal{D}_i)\}_{i=1}^n$. The neural operator \mathcal{G}_θ , parameterized by weights and biases θ across all layers, is optimized by minimizing the relative L^2 error with respect to the reference solutions.

5. Numerical Study. In this section, we present numerical studies of the M-PCNO, with a particular focus on geometric generalization. Specifically,

1. We first investigate the learning of integral operators with translation-invariant kernels defined on variable 2D curves, focusing on the approximation error.
2. We then consider the 2D exterior Laplacian problem, which involves solving a second-kind Fredholm integral equation. Although the corresponding resolvent operator is generally not translation-invariant, it can be approximated via a Neumann series and, consequently, by deep neural operators.
3. Finally, we study a 3D aerodynamics application based on potential flow, demonstrating the effectiveness of M-PCNO on a range of real-world geometries, including aircraft and ground vehicles.

All experiments involve variable computational domains discretized with different numbers of points. To enable consistent and parallelizable processing, all samples (inputs and outputs) are zero-padded to a fixed maximum length. Unless otherwise stated, the M-PCNO architecture consists of 5 multiscale point cloud neural layers (3.14), each with $d_f = 64$ channels. Training is performed using the Adam optimizer [38] with a batch size of 8 over 500 epochs, with the OneCycleLR scheduler [68] for dynamic learning-rate adjustment. All experiments are run on NVIDIA A100 80G GPUs.

5.1. Kernel Integral. In this section, we study the problem of learning integral operators defined on variable two-dimensional curves with translation-invariant kernels. Specifically, we consider

$$\mathcal{G}^\dagger : (f, \partial\Omega) \rightarrow u, \quad u(x) = \int_{\partial\Omega} \kappa(x - y; n_x, n_y) f(y) dy,$$

where $\partial\Omega \subset \mathbb{R}^2$ denotes a variable input curve. When the kernel κ is singular, the integral is understood in the sense of the Cauchy principal value. We consider the following classes of kernels (see also Table 1):

1. Laplacian single layer potential $\kappa : \mathbb{R}^2 \rightarrow \mathbb{R}$

$$(5.1) \quad \kappa(x - y) = -\frac{1}{2\pi} \ln \|x - y\|_2.$$

The operator maps scalar functions $\{f : \mathbb{R}^2 \rightarrow \mathbb{R}\}$ to scalar functions $\{u : \mathbb{R}^2 \rightarrow \mathbb{R}\}$.

2. Laplacian double layer potential $\kappa : \mathbb{R}^2 \times \mathbb{R}^2 \rightarrow \mathbb{R}$

$$(5.2) \quad \kappa(x - y, n_y) = \frac{(x - y) \cdot n_y}{2\pi \|x - y\|_2^2},$$

where n_y denotes the outward normal. The operator maps scalar functions $f : \mathbb{R}^2 \rightarrow \mathbb{R}$ to scalar functions $u : \mathbb{R}^2 \rightarrow \mathbb{R}$.

3. Modified Laplacian double layer potential $\kappa : \mathbb{R}^2 \rightarrow \mathbb{R}^2$

$$(5.3) \quad \kappa(x - y) = \frac{x - y}{2\pi\|x - y\|_2^2}.$$

In this formulation, the normal vector is omitted, and the operator maps scalar functions $f : \mathbb{R}^2 \rightarrow \mathbb{R}$ to vector-valued functions $u : \mathbb{R}^2 \rightarrow \mathbb{R}^2$.

4. Adjoint Laplacian double layer potential $\kappa : \mathbb{R}^2 \times \mathbb{R}^2 \rightarrow \mathbb{R}^2$

$$(5.4) \quad \kappa(x - y, n_x) = \frac{(y - x) \cdot n_x}{2\pi\|x - y\|_2^2},$$

where n_x denotes the outward unit normal at the evaluation point x . The operator maps scalar functions $f : \mathbb{R}^2 \rightarrow \mathbb{R}$ to scalar functions $u : \mathbb{R}^2 \rightarrow \mathbb{R}$.

5. Stokeslet $\kappa : \mathbb{R}^2 \rightarrow \mathbb{R}^{2 \times 2}$

$$(5.5) \quad \kappa(x - y) = \frac{1}{4\pi} \left(-\ln\|x - y\|_2 I_2 + \frac{(x - y)(x - y)^T}{\|x - y\|_2^2} \right).$$

The operator maps from vector-valued functions $\{f : \mathbb{R}^2 \rightarrow \mathbb{R}^2\}$ to vector-valued functions $\{u : \mathbb{R}^2 \rightarrow \mathbb{R}^2\}$.

We evaluate geometric generalization using two datasets, both defined within a bounding box with $l_1 = l_2 = 5$. The first, the *single-curve dataset*, contains problems posed on a single closed curve (see Figure 1-left two). The second, the *two-curve dataset*, contains problems posed on two separate, side-by-side curves, thereby introducing a topological change from one curve to two (see Figure 1-right two). In both datasets, the input function f is sampled from a Gaussian random field. Reference solutions are generated using a panel method (see subsection B.3 for details). We train M-PCNO exclusively on the single-curve dataset and evaluate it on both in-distribution single-curve data and out-of-distribution two-curve data, using 1000 randomly sampled configurations for each test dataset, thereby explicitly testing generalization across changes in geometry and topology.

We consider two network architectures. The first is a single-layer linear model, consisting of a single multiscale point cloud neural layer without an activation function. This model serves as a baseline, demonstrating that the multiscale point cloud neural layer alone can effectively learn the underlying kernel and accurately approximate the associated kernel integral. The second is a 5-layer M-PCNO, used to investigate the benefits of depth and nonlinear composition. We perform comprehensive experiments by varying the truncated mode number $p \in \{8, 16, 32, 64\}$ and training dataset size $n \in \{1000, 2000, 4000, 8000\}$ to quantify the effects of truncation level, data size, and depth on performance.

Representative results for the Laplacian single layer potential are shown in Figure 1, including test samples with median and largest relative errors, from both single-curve and two-curve datasets. Even in the worst case (about 4% relative error on the single-curve test set), the overall error remains small, and is comparable across the two datasets; similar behavior is observed for all kernels. Complete test errors for both datasets are reported in Tables 2 and 3 and visualized in Figure 2. Overall, the results demonstrate that M-PCNO exhibits strong geometric generalization and reveal a fundamental trade-off between model expressivity, which is determined by p and network depth, and the amount of training data required to achieve high accuracy.

1. For the single-layer linear model, the error scales as p^{-1} in both single-curve in-distribution and two-curve out-of-distribution tests (see Figure 2-top), consistent with the theoretical result in Theorem 2.1.

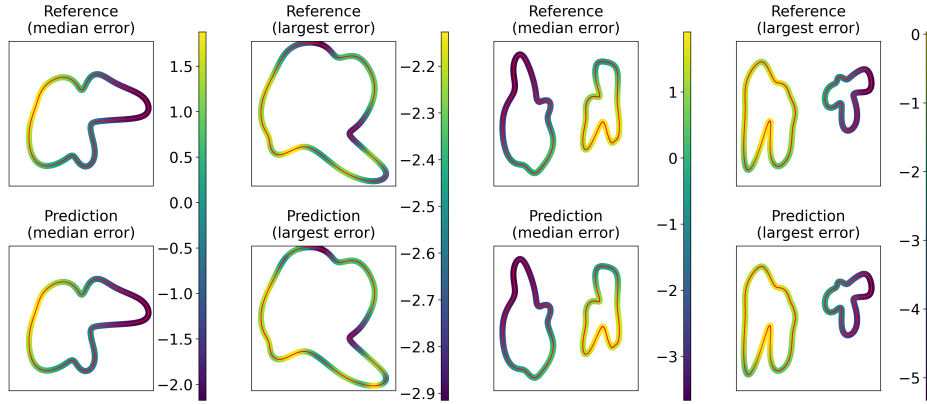


Fig. 1: Representative results for learning the Laplacian single layer potential using a 5-layer M-PCNO with $p = 32$ and $n = 8000$. Each column shows the reference solution (top) and the prediction (bottom) for test cases with median and largest relative errors from the single-curve (left two) and two-curve (right two) test datasets.

Kernel \ p	8	16	32	64				
Laplacian single layer potential	0.4251	0.7979	0.1117	0.2211	0.0597	0.081	0.0593	0.0376
Laplacian double layer potential	10.1761	22.6872	4.5952	13.3501	1.6056	6.3796	0.5962	3.2029
Modified Laplacian double layer potential	10.6008	18.897	4.8453	11.8611	1.7733	5.9475	0.6173	2.5156
Adjoint Laplacian double layer potential	5.4653	10.792	2.2898	6.0529	0.7547	2.8915	0.2933	1.2417
Stokeslet	1.3103	2.3547	0.3562	0.7624	0.1418	0.2538	0.1085	0.1161

Table 2: Kernel integral learning with the single-layer linear model. Relative L^2 test errors ($\times 10^{-2}$) for different truncated mode numbers p , trained on $n = 8000$ single-curve samples. Each entry reports single-curve and two-curve test errors.

2. For 5-layer M-PCNO, the error is generally lower than that of the linear model and still roughly scales as p^{-1} for both single-curve in-distribution and two-curve out-of-distribution tests. However, when p becomes large, the available training data are insufficient to reliably train the more expressive model. As a result, the test error no longer decreases with increasing p and instead plateaus (see Figure 2-top).
3. Increasing the training data size n for 5-layer M-PCNO reduces the error following the scaling law $n^{-\beta}$. For the Laplacian single and double layer potentials and the Stokeslet, the convergence rate reaches the Monte Carlo rate ($\beta = \frac{1}{2}$), while other kernels exhibit slower convergence. We conjecture that kernels with weaker singularities converge more rapidly (see Figure 2-bottom).

5.2. Exterior Laplace Equations. In this section, we study two exterior Laplace problems. The first is a two-dimensional exterior boundary value problem, while the

Kernel \ p	8	16	32	64			
Kernel							
Laplacian single layer potential	0.291	0.7256	0.0934	0.2096	0.0757	0.0828	0.1434
Laplacian double layer potential	1.3531	6.1345	0.6054	3.281	0.2735	1.8418	0.2287
Modified Laplacian double layer potential	0.9628	4.0536	0.5433	2.8021	0.2857	1.4363	0.1993
Adjoint Laplacian double layer potential	1.0068	4.3489	0.5354	2.7218	0.38	1.8117	0.1632
Stokeslet	0.5808	1.6941	0.2254	0.5793	0.1388	0.2525	0.1477
Kernel \ n		1000	2000	4000	8000		
Laplacian single layer potential	0.89	1.1019	0.3475	0.4173	0.1719	0.268	0.0757
Laplacian double layer potential	0.9926	3.8675	0.5247	2.7039	0.3998	2.4095	0.2735
Modified Laplacian double layer potential	0.5943	2.2242	0.4147	1.7736	0.3445	1.6432	0.2857
Adjoint Laplacian double layer potential	0.575	2.1708	0.4826	1.9921	0.4178	1.8831	0.38
Stokeslet	0.8023	1.1355	0.3857	0.5847	0.2187	0.377	0.1388

Table 3: Kernel integral learning with the 5-layer M-PCNO. Relative L^2 test errors ($\times 10^{-2}$) for different truncated mode numbers p , trained on $n = 8000$ single-curve samples (top), and for different single-curve training dataset sizes n with $p = 32$ fixed (bottom). Each entry reports single-curve and two-curve test errors.

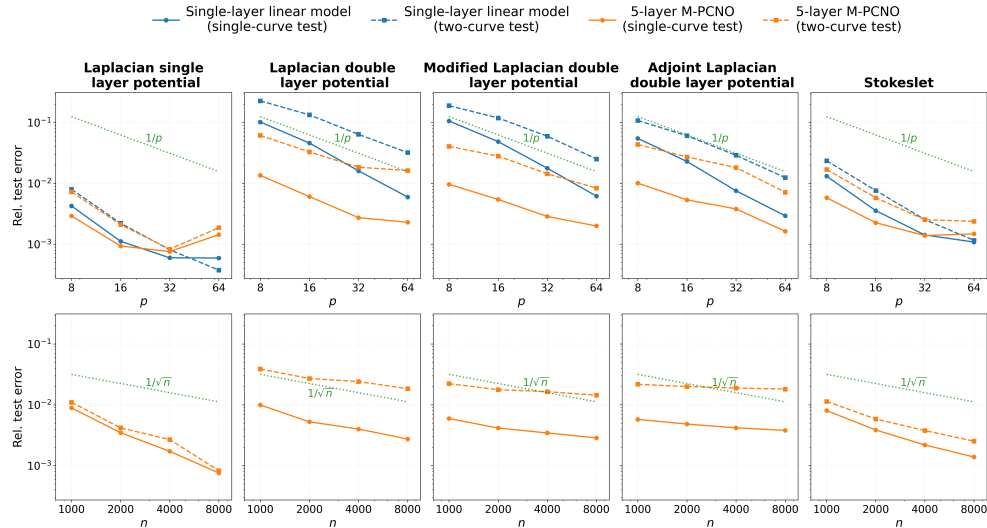


Fig. 2: Kernel integrals: relative test errors as functions of the truncated mode number p with training dataset size $n = 8000$ (top row), and as functions of the training dataset size n with $p = 32$ fixed (bottom row), for different models and test datasets. Each column corresponds to one kernel integral.

second concerns three-dimensional potential flow problem. Both problems involve kernel integrals and their resolvents, i.e., the solution of Fredholm integral equations, which are generally not translation-invariant.

5.2.1. Exterior Neumann Problem. We consider the exterior Laplace equation on $\Omega^c = \mathbb{R}^2 \setminus \Omega$, where $\partial\Omega$ is smooth:

$$(5.6) \quad \begin{aligned} \Delta\Phi &= 0 && \text{in } \Omega^c, \\ \frac{\partial\Phi(x)}{\partial n_x} &= f(x) && \text{on } \partial\Omega, \quad \int_{\partial\Omega} f(x)dx = 0, \\ \lim_{|x| \rightarrow \infty} \Phi(x) &= 0. \end{aligned}$$

Our goal is to learn the Neumann-to-Dirichlet map on $\partial\Omega$:

$$\mathcal{G}^\dagger : (f, \partial\Omega) \rightarrow \Phi(x)|_{\partial\Omega},$$

where $\{f : \mathbb{R}^2 \rightarrow \mathbb{R}\}$ and $\{\Phi : \mathbb{R}^2 \rightarrow \mathbb{R}\}$. The solution admits the single layer potential representation

$$(5.7) \quad \Phi(x) = \int_{\partial\Omega} \sigma(y) \kappa(x - y) dy,$$

where $\kappa(x - y) = -\frac{1}{2\pi} \ln \|x - y\|_2$ is the Laplacian single layer potential kernel and σ is an unknown density on $\partial\Omega$. The density σ satisfies the following Fredholm integral equation of the second kind on $\partial\Omega$:

$$(5.8) \quad f(x) = -\frac{1}{2} \sigma(x) + \int_{\partial\Omega} \sigma(y) \nabla_x \kappa(x - y) \cdot n_x dy.$$

The experimental setup, including the geometries and input functions, is identical to that in [subsection 5.1](#). The Neumann-to-Dirichlet map involves the composition of the operators in (5.7) and (5.8). Since the resolvent associated with (5.8) is generally not translation-invariant, it cannot be represented by a single convolution operator. Instead, it admits a Neumann series expansion involving repeated operator compositions, so sufficient depth is required for accurate approximation.

We evaluate a 5-layer M-PCNO by varying the truncated mode number $p \in \{8, 16, 32, 64\}$ and the training dataset size $n \in \{1000, 2000, 4000, 8000\}$. Test errors on both the single-curve in-distribution and two-curve out-of-distribution datasets are reported in [Table 4](#) and visualized in [Figure 3](#). The overall trends are consistent with the previous section. However, compare with learning a single kernel integral, approximating the Neumann-to-Dirichlet map requires the network to represent the resolvent via repeated compositions, which makes optimization more challenging and increases the risk of overfitting on the single-curve training distribution without capturing the underlying operator structure. For the two-curve tests, increasing the truncated mode number reduces the test error, with an empirical decay rate slightly slower than p^{-1} ; for $p = 64$, limited training data prevent further improvement, and performance deteriorates. For the single-curve in-distribution tests, the errors are significantly smaller, and no clear dependence on p is observed. We attribute this behavior to overfitting on the in-distribution data; consequently, strong performance on such test data does not necessarily indicate good generalization. Moreover, increasing the training data size n reduces the error approximately following the scaling law $n^{-1/2}$ for both single-curve in-distribution and two-curve out-of-distribution tests.

$p \setminus n$	1000	2000	4000	8000
8	3.4427	13.5705	2.2997	13.5514
16	2.7867	10.0941	1.7473	8.8995
32	3.5967	9.3321	2.1442	7.3943
64	4.5981	10.7413	2.9173	9.52
			1.2328	13.024
			0.9289	8.1034
			0.9217	4.9039
			1.0939	6.1703

Table 4: Neumann-to-Dirichlet map for the exterior Laplacian learned with a 5-layer M-PCNO. Relative L^2 test errors ($\times 10^{-2}$) for different single-curve training dataset sizes n and truncated mode numbers p . Each entry reports single-curve and two-curve test errors.

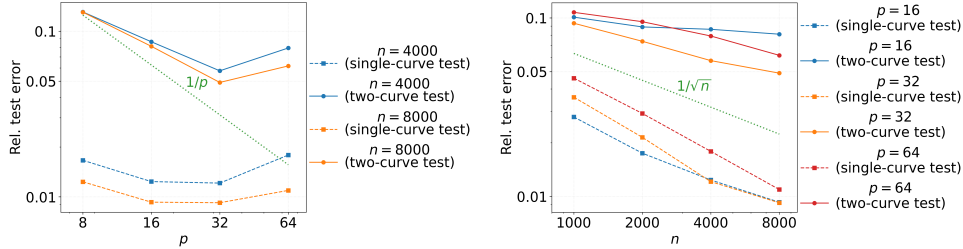


Fig. 3: Neumann-to-Dirichlet map for the exterior Laplacian learned with a 5-layer M-PCNO: relative L^2 test errors as functions of the truncated mode number p (left) and the training dataset size n (right).

5.2.2. Potential Flow Problem. Finally, we consider incompressible, inviscid flow past a three-dimensional object $\Omega \in \mathbb{R}^3$, governed by the steady Euler equations:

$$(5.9a) \quad \nabla \cdot (\rho v) = 0,$$

$$(5.9b) \quad \nabla \cdot (\rho v v^T + pI) = 0,$$

where ρ is the fluid density, v is the velocity field, and p is the pressure. Under the potential flow assumption—constant density ($\rho = \text{const.}$) and zero vorticity ($\nabla \times v = 0$)—the velocity field can be expressed as the gradient of a scalar potential $v = \nabla \Phi$. In this case, (5.9a) reduces to the exterior Laplace problem

$$(5.10) \quad \Delta \Phi = 0 \quad \text{in} \quad \mathbb{R}^d \setminus \Omega,$$

with the far-field velocity condition

$$(5.11) \quad \lim_{|x| \rightarrow \infty} \nabla \Phi(x) = \lim_{|x| \rightarrow \infty} v(x) = v_\infty,$$

and the no-penetration boundary condition

$$(5.12) \quad v(x) \cdot n_x = \frac{\partial \Phi(x)}{\partial n_x} = 0 \quad \text{on} \quad \partial \Omega,$$

where n_x denotes the outward unit normal. Combining (5.9) with $\nabla \times v = 0$ yields the Bernoulli's law,

$$(5.13) \quad \nabla \left(p + \frac{\rho v^2}{2} \right) = 0 \quad \text{or} \quad p + \frac{\rho v^2}{2} = \text{const},$$

and the pressure coefficient is

$$(5.14) \quad C_p(x) = \frac{p(x) - p_\infty}{\frac{1}{2}\rho\|v_\infty\|_2^2} = 1 - \frac{\|v\|_2^2}{\|v_\infty\|_2^2}.$$

Our goal is to learn the aerodynamic map,

$$\mathcal{G}^\dagger : (v_\infty, \partial\Omega) \rightarrow C_p|_{\partial\Omega}.$$

which maps the freestream velocity $v_\infty \in \mathbb{R}^3$ and the geometry to the boundary pressure coefficient $\{C_p : \mathbb{R}^3 \rightarrow \mathbb{R}\}$.

In this work, we focus on the no-lifting solution satisfying

$$(5.15) \quad \lim_{|x| \rightarrow \infty} \Phi(x) - v_\infty \cdot x = 0,$$

Following the panel method [32], we write

$$(5.16) \quad \Phi(x) = \Phi_\infty(x) + \Phi_s(x).$$

where

$$(5.17) \quad \Phi_\infty(x) = v_\infty \cdot x, \quad \Phi_s(x) = \int_{\partial\Omega} \sigma(y) \kappa(x - y) dy, \quad \kappa(x - y) = \frac{1}{4\pi\|x - y\|_2}.$$

Here σ is an unknown density on $\partial\Omega$. Since Φ already satisfies the far-field condition, σ is determined by enforcing the no-penetration condition (5.12):

$$(5.18) \quad v_\infty \cdot n_x - \frac{1}{2}\sigma(x) + \int_{\partial\Omega} \sigma(y) \nabla_x \kappa(x - y) dy \cdot n_x = 0.$$

Once σ is obtained, the surface velocity is computed as

$$(5.19) \quad v = \nabla\Phi(x) = v_\infty + \int_{\partial\Omega} \sigma(y) \nabla_x \kappa(x - y) dy,$$

and C_p follows from (5.14).

We construct a dataset of diverse three-dimensional geometries to train and evaluate our model. The dataset consists of two categories: cars and aircraft. The car subset (about 5,000 samples), including fastback, notchback, and estateback designs, is derived from DrivAerNet++[16] (see Figure 4). The aircraft subset (about 6,000 samples) is generated using NASA's Open Vehicle Sketch Pad (OpenVSP). Baseline aircraft designs, including a fighter jet, a turboprop aircraft, and a commercial airliner, are obtained from the OpenVSP Airshow (<https://airshow.openvsp.org/>) and modified to form reference templates. Stochastic perturbations are then applied to the shape parameters of these templates, yielding a diverse range of aerodynamic configurations. All surface meshes are converted to triangular meshes and decimated to about 40,000 elements, then isotropically scaled to fit within the bounding box $[-1, 1]^3$. The surface pressure coefficients C_p are computed using the panel method with a freestream inflow condition $v_\infty = [1, 0, 0]$. Note that scaling the inflow velocity does not affect C_p .

We train 5-layer M-PCNO models with a fixed truncated mode number $p = 16$ using training datasets of size $n \in \{1000, 2000, 4000\}$, each randomly sampled from the

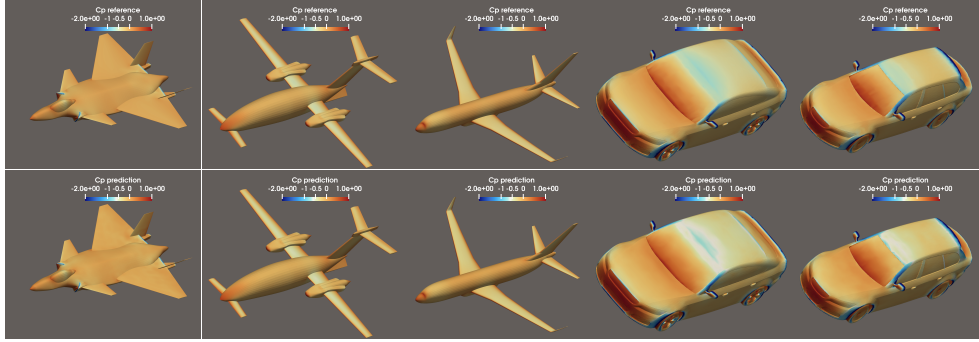


Fig. 4: Representative results for the potential flow problem using a 5-layer M-PCNO with $p = 16$ and $n = 4000$. Each column shows the reference solution (top) and the prediction (bottom) for test cases with the largest relative error (leftmost, fighter jet), the median relative error (left-middle, turboprop), and three randomly selected samples.

full dataset. Performance is evaluated on a separate test set of 500 randomly sampled configurations. The relative L^2 test errors reported in Table 5 follow a scaling law proportional to $n^{-0.167}$. Representative results for the model trained with $n = 4000$ are shown in Figure 4. The mean relative L^2 test error is 8.054% across this diverse geometric dataset. The worst-case example (fighter jet) attains a relative L^2 error of roughly 30%, primarily because its pressure coefficient has small magnitude, so modest absolute discrepancies translate into large relative errors; the same effect is observed across the fighter-jet category. Overall, the predicted pressure coefficients agree closely with the reference solutions. In terms of computational cost, for problems of this scale (about 40,000 elements), M-PCNO inference takes under 10 seconds on a CPU and 0.2 second on a GPU. These results demonstrate that a single surrogate model has the potential to accommodate a wide range of geometries and significantly accelerate large-scale 3D aerodynamic simulations.

n	1000	2000	4000
Rel. test error ($\times 10^{-2}$)	10.15	8.557	8.054

Table 5: Potential flow problem with a 5-layer M-PCNO. Relative L^2 test errors ($\times 10^{-2}$) for different training dataset sizes n with the truncated mode number fixed at $p = 16$.

6. Conclusion. We study neural operators on variable and nonparametric geometries from a kernel integral perspective, in which learning solution operators amounts to approximating geometry-dependent, potentially singular kernels and their associated operations. This framework clarifies the mechanism of geometric generalization and guides the design of the M-PCNO, for which we also establish corresponding approximation error bounds. Numerical results demonstrate robust generalization across diverse geometries with favorable computational efficiency. Several promising directions for future research remain. On the theoretical side, an important question is how the scaling laws relating test error to training data size depend on problem

properties. On the application side, extending and improving the present approach to nonlinear problems, especially challenging fluid dynamics problems involving shocks, turbulence, and engineering design, is a key direction.

Acknowledgments. We acknowledge the support of the high-performance computing platform of Peking University.

Appendix A. Proof of Theorem 2.1.

Proof. Since $\kappa \in L^1(B_2)$ and is periodic, it has Fourier coefficients

$$(A.1) \quad \hat{\kappa}_k = \int_{B_2} \kappa(x) e^{-2\pi i k \cdot x} dx \leq \|\kappa\|_{L^1(B_2)}, \quad k \in \mathbb{Z}^d.$$

Next, we show that κ_{long} is well defined on \mathbb{R}^d and bounded. Observe that

$$\int_{\mathbb{R}^d} |\kappa(x - y)| \rho_\delta(y) dy = \sum_{n \in \mathbb{Z}^d} \int_{[-\frac{1}{2}, \frac{1}{2}]^d + n} |\kappa(x - y)| \rho_\delta(y) dy.$$

Using periodicity of κ , we obtain

$$(A.2) \quad \begin{aligned} \int_{\mathbb{R}^d} |\kappa(x - y)| \rho_\delta(y) dy &\leq \|\kappa\|_{L^1(B_2)} \sum_{n \in \mathbb{Z}^d} \max_{B_2 + n} \rho_\delta(y) \\ &\leq \|\kappa\|_{L^1(B_2)} \frac{2^d}{(2\pi\delta^2)^{d/2}} \sum_{n_1=0}^{\infty} \cdots \sum_{n_d=0}^{\infty} \max_{[-\frac{1}{2}, \frac{1}{2}]^d + n} e^{-\frac{\|y\|_2^2}{2\delta^2}} \\ &\leq \|\kappa\|_{L^1(B_2)} \frac{2^d}{(2\pi\delta^2)^{d/2}} \left(1 + \sum_{n_1=1}^{\infty} e^{-\frac{1}{2\delta^2}(n_1 - \frac{1}{2})^2}\right)^d \\ &\leq C(\kappa, d, \delta). \end{aligned}$$

In the second inequality, we consider n in the first quadrant. In the third inequality, we use the component-wise estimate $\|y\|_2^2 = \sum_{i=1}^d y_i^2$, take the maximum in each coordinate direction, and bound each component separately. So $\kappa_{\text{long}} = \kappa * \rho_\delta$ is well-defined everywhere and is bounded. Next, we establish each property separately.

Property 1: For the mollified kernel κ_{long} , we compute its Fourier coefficients:

$$(A.3) \quad \begin{aligned} \widehat{\kappa_{\text{long}}}_k &= \int_{B_2} \kappa_{\text{long}} e^{-2\pi i k \cdot x} dx = \int_{B_2} dx \int_{\mathbb{R}^d} \kappa(x - y) \rho_\delta(y) e^{-2\pi i k \cdot x} dy \\ &= \int_{\mathbb{R}^d} \rho_\delta(y) e^{-2\pi i k \cdot y} \int_{B_2 - y} \kappa(x) e^{-2\pi i k \cdot x} dx dy \\ &= \hat{\kappa}_k e^{-2\pi^2 \delta^2 \|\kappa\|_2^2}. \end{aligned}$$

The exchange of integrals is justified by Tonelli's and Fubini's theorems, using the bound in (A.2). Hence, mollification damps the Fourier coefficients of κ by a Gaussian factor. We now derive an L^∞ bound on the Fourier tail of κ_{long} , i.e., on the partial

sum over all modes $k \in \mathbb{Z}^d : \|k\|_\infty > p$:

$$\begin{aligned}
\left\| \sum_{\|k\|_\infty > p} \widehat{\kappa_{\text{long}}}_k e^{2\pi i k \cdot x} \right\|_{L^\infty(B_2)} &\leq \sum_{\|k\|_\infty > p} |\widehat{\kappa_{\text{long}}}_k| \\
&\leq \|\kappa\|_{L^1(B_2)} 2^d d \sum_{k_1=0}^{\infty} \dots \sum_{k_{d-1}=0}^{\infty} \sum_{k_d=p+1}^{\infty} e^{-2\pi^2 \delta^2 \|k\|_2^2} \\
(A.4) \quad &\leq \|\kappa\|_{L^1(B_2)} 2^d d \left(1 + \int_0^\infty e^{-2\pi^2 \delta^2 k^2} dk\right)^{d-1} \left(\int_p^\infty e^{-2\pi^2 \delta^2 k^2} dk\right) \\
&\leq \|\kappa\|_{L^1(B_2)} 2^d d \left(1 + \frac{1}{2\sqrt{2\pi}\delta}\right)^{d-1} \frac{e^{-2\pi^2 \delta^2 p^2}}{4\pi^2 \delta^2 p} \quad \text{using } \delta < \frac{1}{2} \\
&\leq \frac{d\|\kappa\|_{L^1(B_2)}}{2\pi^2} \left(1 + \frac{1}{\sqrt{2\pi}}\right)^{d-1} \frac{e^{-2\pi^2 \delta^2 p^2}}{\delta^{d+1} p}.
\end{aligned}$$

For the second inequality, we substitute (A.3) and consider k in the first quadrant with $k_d > p$. For the third inequality, we use the decomposition $\|k\|_2^2 = \sum_i k_i^2$ and bound each component separately. This completes the proof of (2.8).

Property 2: For the short-range component, let $0 < \delta_p < \frac{1}{2}$. For every $x \in B_2$ such that $\|x\|_2 > \delta_p$, we decompose the integral into two regions:

$$\begin{aligned}
\kappa_{\text{short}}(x) &= \int_{\mathbb{R}^d} (\kappa(x) - \kappa(x-y)) \rho_\delta(y) dy \\
(A.5) \quad &= \int_{\|y\|_2 < \delta_p} (\kappa(x) - \kappa(x-y)) \rho_\delta(y) dy + \int_{\|y\|_2 > \delta_p} (\kappa(x) - \kappa(x-y)) \rho_\delta(y) dy.
\end{aligned}$$

For the first term in (A.5), a Taylor expansion of $\kappa(x-y)$ gives, for some $\theta \in (0, 1)$,

$$\begin{aligned}
(A.6) \quad &\left| \int_{\|y\|_2 < \delta_p} (\kappa(x) - \kappa(x-y)) \rho_\delta(y) dy \right| \\
&\leq \left| \int_{\|y\|_2 < \delta_p} (\nabla \kappa(x) \cdot y) \rho_\delta(y) dy \right| + \frac{1}{2} \int_{\|y\|_2 < \delta_p} \|\nabla^2 \kappa(x - \theta(x, y)y)\|_2 \|y\|_2^2 \rho_\delta(y) dy \\
&\leq 0 + \frac{d\delta^2}{2} \sup_{\|z\|_2 > \|x\|_2 - \delta_p} \|\nabla^2 \kappa(z)\|_2 \quad \text{using assumption (2.6)} \\
&\leq \frac{d\delta^2}{2} C \left(\frac{1}{\|x\|_2 - \delta_p} \right)^{d+1}.
\end{aligned}$$

In the second inequality, we use $\|x - \theta y\|_2 \geq \|x\|_2 - \delta_p$ and $\int_{\mathbb{R}^d} \|y\|_2^2 \rho_\delta(y) dy = \text{tr}[\int_{\mathbb{R}^d} yy^T \rho_\delta(y) dy] = d\delta^2$. For the second term in (A.5), we have the decomposition

$$\begin{aligned}
(A.7) \quad &\left| \int_{\|y\|_2 > \delta_p} (\kappa(x) - \kappa(x-y)) \rho_\delta(y) dy \right| \\
&\leq \int_{\|y\|_2 > \delta_p} |\kappa(x)| \rho_\delta(y) dy + \int_{\|y\|_2 > \delta_p} |\kappa(x-y)| \rho_\delta(y) dy.
\end{aligned}$$

The first term in (A.7) is a Gaussian tail. Using spherical coordinates, we have

$$\begin{aligned}
|\kappa(x)| \int_{\|y\|_2 > \delta_p} \rho_\delta(y) dy &= |\kappa(x)| \frac{1}{(2\pi)^{d/2}} \int_{\|z\|_2 > \delta_p/\delta} e^{-\frac{\|z\|_2^2}{2}} dz \\
(A.8) \quad &= |\kappa(x)| \frac{2\pi^{d/2}}{(2\pi)^{d/2}\Gamma(d/2)} \int_{\delta_p/\delta}^\infty r^{d-1} e^{-\frac{r^2}{2}} dr \\
&\leq |\kappa(x)| \frac{2^{1-d/2}}{\Gamma(d/2)} 2^{d/2-1} \Gamma\left(\frac{d}{2}, \frac{\delta_p^2}{2\delta^2}\right) \quad \text{using assumption (2.6)} \\
&\leq \frac{C}{\|x\|_2^{d-1}} \frac{1}{\Gamma(d/2)} \Gamma\left(\frac{d}{2}, \frac{\delta_p^2}{2\delta^2}\right),
\end{aligned}$$

where Γ is the Gamma function. To bound the second term in (A.7), we partition \mathbb{R}^d into unit cubes and use the periodicity of κ :

$$\begin{aligned}
(A.9) \quad \int_{\|y\|_2 > \delta_p} |\kappa(x-y)| \rho_\delta(y) dy &= \sum_{n \in \mathbb{Z}^d} \int_{\{\|y\|_2 > \delta_p\} \cap \{[-\frac{1}{2}, \frac{1}{2}]^d + n\}} |\kappa(x-y)| \rho_\delta(y) dy \\
&\leq \|\kappa\|_{L^1(B_2)} \sum_{n \in \mathbb{Z}^d} \max_{\{\|y\|_2 > \delta_p\} \cap \{[-\frac{1}{2}, \frac{1}{2}]^d + n\}} \rho_\delta(y) \\
&= \|\kappa\|_{L^1(B_2)} \left(\frac{1}{(2\pi\delta^2)^{d/2}} e^{-\frac{\delta_p^2}{2\delta^2}} + \sum_{n \in \mathbb{Z}^d \setminus \{0\}} \max_{[-\frac{1}{2}, \frac{1}{2}]^d + n} \rho_\delta(y) \right) \\
&\leq \|\kappa\|_{L^1(B_2)} \left(\frac{1}{(2\pi\delta^2)^{d/2}} e^{-\frac{\delta_p^2}{2\delta^2}} + \frac{2^d d}{(2\pi\delta^2)^{d/2}} \sum_{n_1=0}^\infty \dots \sum_{n_{d-1}=0}^\infty \sum_{n_d=1}^\infty \max_{[-\frac{1}{2}, \frac{1}{2}]^d + n} e^{-\frac{\|y\|_2^2}{2\delta^2}} \right) \\
&\leq \|\kappa\|_{L^1(B_2)} \left(\frac{1}{(2\pi\delta^2)^{d/2}} e^{-\frac{\delta_p^2}{2\delta^2}} + \frac{2^d d}{(2\pi\delta^2)^{d/2}} \left(1 + \sum_{n_1=1}^\infty e^{-\frac{1}{2\delta^2}(n_1 - \frac{1}{2})^2}\right)^{d-1} \sum_{n_d=1}^\infty e^{-\frac{1}{2\delta^2}(n_d - \frac{1}{2})^2} \right) \\
&\leq \|\kappa\|_{L^1(B_2)} \left(\frac{1}{(2\pi\delta^2)^{d/2}} e^{-\frac{\delta_p^2}{2\delta^2}} + \frac{2^d d}{(2\pi\delta^2)^{d/2}} \frac{e^{-\frac{1}{8\delta^2}}}{(1 - e^{-\frac{1}{8\delta^2}})^d} \right) \quad \text{using } \delta_p < \frac{1}{2} \\
&\leq \frac{\|\kappa\|_{L^1(B_2)}}{(2\pi\delta^2)^{d/2}} \left(1 + \frac{2^d d}{(1 - e^{-\frac{1}{8\delta^2}})^d}\right) e^{-\frac{\delta_p^2}{2\delta^2}}.
\end{aligned}$$

In the second inequality, we consider n in the first quadrant with $n_d \geq 1$. In the third inequality, we use the component-wise estimate $\|y\|_2^2 = \sum_{i=1}^d y_i^2$, take the maximum in each coordinate direction, and bound each component separately. In the fourth inequality, we use the fact that $(2n_i - 1)^2 \geq n_i$, $\forall n_i \geq 1$, and consequently,

$$\sum_{n_i=1}^\infty e^{-\frac{1}{2\delta^2}(\frac{2n_i-1}{2})^2} \leq \sum_{n_i=1}^\infty e^{-\frac{n_i}{8\delta^2}} = \frac{e^{-\frac{1}{8\delta^2}}}{1 - e^{-\frac{1}{8\delta^2}}}.$$

Substituting (A.6), (A.8), and (A.9) into (A.5) and choosing

$$(A.10) \quad \delta_p = (1 - \delta^\alpha) \|x\|_2 < \|x\|_2 \quad (\alpha > 0),$$

yields the following bound for the short-range component, valid for any $x \in B_2 \setminus \{0\}$:

$$|\kappa_{\text{short}}(x)| \leq \frac{dC\delta^{2-\alpha(d+1)}}{2\|x\|_2^{d+1}} + \frac{\|\kappa\|_{L^1(B_2)}}{(2\pi)^{d/2}} \left(1 + \frac{2^d d}{(1 - e^{-\frac{1}{8\delta^2}})^d}\right) \frac{e^{-\frac{(1-\delta^\alpha)^2\|x\|_2^2}{2\delta^2}}}{\delta^d} + \frac{C}{\|x\|_2^{d-1}\Gamma(d/2)} \Gamma\left(\frac{d}{2}, \frac{(1-\delta^\alpha)^2}{2\delta^2} \|x\|_2^2\right).$$

Bringing the upper bound for the Gamma function from [Lemma A.1](#) into the last term, we obtain, for any $\|x\|_2 \geq \delta$:

$$\begin{aligned} |\kappa_{\text{short}}(x)| &\leq \frac{dC\delta^{2-\alpha(d+1)}}{2\|x\|_2^{d+1}} + \left(\frac{\|\kappa\|_{L^1(B_2)}}{(2\pi)^{d/2}} \left(1 + \frac{2^d d}{(1 - e^{-\frac{1}{8\delta^2}})^d} \right) + \frac{CC_{d/2}}{\Gamma(\frac{d}{2})} \left(\frac{(1-\delta^\alpha)^{d-2}}{2^{d/2-1}} \frac{\delta^2}{\|x\|_2} + \frac{2\delta^{d+2}}{(1-\delta^\alpha)^2\|x\|_2^{d+1}} \right) \right) \frac{e^{-\frac{1}{2}(1-\delta^\alpha)^2\frac{\|x\|_2^2}{\delta^2}}}{\delta^d} \\ &\leq \frac{dC\delta^{2-\alpha(d+1)}}{2\|x\|_2^{d+1}} + \left(\frac{\|\kappa\|_{L^1(B_2)}}{(2\pi)^{d/2}} \left(1 + \frac{2^d d}{(1 - e^{-1/2})^d} \right) + \frac{CC_{d/2}}{\Gamma(\frac{d}{2})} \left(\frac{1}{2^{d/2}} + \frac{1}{(1-2^{-\alpha})^2} \right) \right) \frac{e^{-\frac{1}{2}(1-\delta^\alpha)^2\frac{\|x\|_2^2}{\delta^2}}}{\delta^d}. \end{aligned}$$

Here the final inequality follows from the assumption $\|x\|_2 \geq \delta$ and $\delta < \frac{1}{2}$.

Property 3: Assume that the short-range component κ_{short} can be approximated locally on B_ϵ by a function $\tilde{\kappa}_{\text{short}}$ with accuracy $\mathcal{O}(\epsilon^{d+q})$:

$$(A.11) \quad \|\tilde{\kappa}_{\text{short}} - \kappa_{\text{short}}\|_{L^1(B_\epsilon)} \leq M\epsilon^{d+q},$$

for some $q > 0$ and constant $M > 0$. Using the decomposition above, we approximate κ by

$$(A.12) \quad \tilde{\kappa}(x) = \sum_{\|k\|_\infty \leq p} \widehat{\kappa_{\text{long}}}_k e^{2\pi i k \cdot x} + \mathbb{1}_{B_\epsilon} \tilde{\kappa}_{\text{short}}(x).$$

Applying the error bounds in [\(A.11\)](#), [\(2.8\)](#), and [\(2.9\)](#) and using $|B_2| = 1$, we decompose the L^1 error into three contributions:

$$\begin{aligned} (A.13) \quad \|\tilde{\kappa} - \kappa\|_{L^1(B_2)} &\leq \left\| \sum_{\|k\|_\infty \leq p} \widehat{\kappa_{\text{long}}}_k e^{2\pi i k \cdot x} - \kappa_{\text{long}} \right\|_{L^1(B_2)} + \|\kappa_{\text{short}}\|_{L^1(B_2 \setminus B_\epsilon)} + \|\tilde{\kappa}_{\text{short}} - \kappa_{\text{short}}\|_{L^1(B_\epsilon)} \\ &\leq \frac{C_{\text{long}}}{\delta^{d+1} p} e^{-2\pi^2 \delta^2 p^2} + \frac{dC\delta^{2-\alpha(d+1)}}{2\epsilon^{d+1}} + C_{\text{short}} \frac{e^{-\frac{(1-\delta^\alpha)^2 \epsilon^2}{2\delta^2}}}{\delta^d} + M\epsilon^{d+q}. \end{aligned}$$

We then choose δ and ϵ to balance the two polynomially decaying terms in [\(A.13\)](#) while ensuring that the exponential terms decay rapidly. Specifically, set

$$(A.14) \quad \delta = p^{-\gamma}, \quad \epsilon = \delta^t = p^{-\gamma t}, \quad t = \frac{2 - \alpha(d+1)}{q + 2d + 1},$$

with parameters $\gamma \in (0, 1)$, $\alpha \in (0, \frac{2}{d+1})$, and $p > 2^{\frac{1}{\gamma}}$. These choices ensure $\delta < \frac{1}{2}$ and $\epsilon \geq \delta$ (since $t \in (0, 1)$), as required for the short-range approximation [\(2.9\)](#). Substituting into [\(A.13\)](#) yields

$$\begin{aligned} (A.15) \quad \|\tilde{\kappa} - \kappa\|_{L^1(B_2)} &\leq \frac{C_{\text{long}}}{\delta^{d+1} p} e^{-2\pi^2 \delta^2 p^2} + C_{\text{short}} \delta^{-d} e^{-\frac{1}{2}(1-\delta^\alpha)^2 \delta^{2t-2}} + \left(\frac{dC}{2} + M \right) \delta^{t(q+d)} \\ &\leq C_{\text{long}} p^{-1+\gamma(d+1)} e^{-2\pi^2 p^{2-2\gamma}} + C_{\text{short}} p^{d\gamma} e^{-\frac{1}{2}(1-\delta^\alpha)^2 p^{\gamma(2-2t)}} + \left(\frac{dC}{2} + M \right) p^{-\gamma t(q+d)}. \end{aligned}$$

The bound [\(A.15\)](#) consists of two exponentially decaying terms and one polynomially decaying term. For sufficiently large p , the polynomial term

$$p^{-\gamma \left(1 + \frac{q-1-\alpha(d+1)(q+d)}{q+2d+1} \right)}$$

dominates the overall error. \square

LEMMA A.1. *For any $\alpha > 0$, there exists a constant C_α depending only on α such that for every $x > 0$*

$$(A.16) \quad \Gamma(\alpha, x) = \int_x^\infty t^{\alpha-1} e^{-t} dt \leq C_\alpha(x^{\alpha-1} + x^{-1})e^{-x}.$$

Proof. We prove the claim by induction. For every $n \in \mathbb{Z}_+$, we show that

$$\forall \alpha \in (n-1, n], \quad \exists C_\alpha \quad \text{such that} \quad \Gamma(\alpha, x) \leq C_\alpha(x^{\alpha-1} + x^{-1})e^{-x} \quad \forall x > 0.$$

For the base case, let $n = 1$, so $\alpha \in (0, 1]$. Then

$$\Gamma(\alpha, x) = \int_x^\infty t^{\alpha-1} e^{-t} dt \leq x^{\alpha-1} \int_x^\infty e^{-t} dt = x^{\alpha-1} e^{-x},$$

here the inequality uses $t^{\alpha-1} \leq x^{\alpha-1}$ for all $t \geq x > 0$, which holds when $\alpha \in (0, 1]$. For the induction step, assume the claim holds for $n = k-1 \in \mathbb{Z}_+$. For $n = k \in \mathbb{Z}_+$, integration by parts gives

$$\begin{aligned} \Gamma(\alpha, x) &= \int_x^\infty t^{\alpha-1} e^{-t} dt = -t^{\alpha-1} e^{-t} \Big|_x^\infty + (\alpha-1) \int_x^\infty t^{\alpha-2} e^{-t} dt \\ &\leq x^{\alpha-1} e^{-x} + (\alpha-1) C_{\alpha-1} (x^{\alpha-2} + x^{-1}) e^{-x} \\ &\leq (1 + 2(\alpha-1) C_{\alpha-1}) (x^{\alpha-1} + x^{-1}) e^{-x}. \end{aligned}$$

Here the last inequality uses $x^{\alpha-2} + x^{-1} \leq 2(x^{\alpha-1} + x^{-1})$ under the condition $\alpha > 1$, since $x^{\alpha-2} \leq x^{\alpha-1}$ when $x \geq 1$ and $x^{\alpha-2} \leq x^{-1}$ when $x < 1$. By induction on n , the result holds for all $\alpha > 0$. \square

Appendix B. Kernel Analysis. In this section, we analyze the kernels used throughout this work (see, e.g., Table 1). First, in subsection B.1, we verify that these kernels satisfy the regularity assumptions required for Theorem 2.1. Next, in subsection B.2, we derive local short-range asymptotic approximations of these kernel integrals. The analysis shows that the leading-order contribution takes the form

$$(B.1) \quad \int_{\partial \cap B_\epsilon(x)} \kappa'(x-y) f(y) dy = M_0(x) f(x) + M_1(x) \cdot \nabla_{\mathcal{D}} f(x) + \mathcal{O}(\epsilon^d),$$

where the remainder is higher order in ϵ (at least one order beyond the intrinsic dimension of $\partial\Omega$). The geometric moments M_0 and M_1 are polynomial functions of the outward normal n_x and the curvature $\text{tr}[\nabla_{\mathcal{D}} n_x]$. Finally, in subsection B.3, we present a panel method evaluation of the kernel integrals used in subsection 5.1.

B.1. Kernel Properties Verification. In this subsection, we verify that the kernels in Table 1 satisfy the regularity assumptions in Theorem 2.1. Specifically, for a bounded box $B_2 = \prod_{i=1}^d [-l_i, l_i]$, we require $\kappa \in L^1(B_2) \cap C^2(B_2 \setminus \{0\})$ and the pointwise bounds

$$(B.2) \quad \|\nabla^k \kappa(x)\|_2 \leq \frac{C}{\|x\|_2^{k+d-1}}, \quad k = 0, 1, 2, \quad x \in B_2 \setminus \{0\},$$

for some constant $C > 0$. All kernels are smooth away from the origin. After rescaling the box if necessary (absorbing the scaling into the constant C), it suffices to verify (B.2) for $0 < \|x\|_2 \leq 1$. Let $r = \|x\|_2$. For $0 \leq r \leq 1$, we use the elementary inequalities $|\log r| \leq r^{-1}$ and $r^{-m} \leq r^{-(m+1)}$.

- For the 2D Laplacian single layer kernel $\kappa(x) = -(2\pi)^{-1} \log r$, we have

$$\nabla \kappa(x) = -(2\pi)^{-1} \frac{x}{r^2}, \quad \nabla^2 \kappa(x) = -(2\pi)^{-1} \left(\frac{1}{r^2} I_2 - \frac{2}{r^4} x x^T \right).$$

Hence, for $0 < r \leq 1$, $|\kappa(x)| \leq r^{-1}$, $\|\nabla \kappa(x)\|_2 \lesssim r^{-1} \leq r^{-2}$, $\|\nabla^2 \kappa(x)\|_2 \lesssim r^{-2} \leq r^{-3}$.

- For the 2D modified Laplacian double layer kernel $\kappa(x) = \frac{x}{2\pi r^2}$, we have

$$\nabla \kappa(x) = \frac{1}{2\pi} \left(\frac{1}{r^2} I_2 - \frac{2}{r^4} x x^T \right), \quad \nabla^2 \kappa(x)[h] = \frac{1}{2\pi} \left(\frac{8x^T h}{r^6} x x^T - \frac{2(xh^T + hx^T + x^T h I_2)}{r^4} \right).$$

Hence, for $0 < r \leq 1$, we have $\|\kappa(x)\|_2 \lesssim r^{-1}$, $\|\nabla \kappa(x)\|_2 \lesssim r^{-2}$, and $\|\nabla^2 \kappa(x)\|_2 \lesssim r^{-3}$. The Laplacian double layer and adjoint double layer kernels are obtained by multiplying by bounded unit normals (e.g., n_x and n_y), so they have the same singular order and satisfy the same bounds.

- For the 2D Stokeslet, $\kappa(x) = \frac{1}{4\pi} \left(-\log r I_2 + \frac{x x^T}{r^2} \right)$, we have

$$\begin{aligned} \nabla \kappa(x)[h] &= \frac{1}{4\pi} \left(-\frac{x^T h}{r^2} I_2 + \frac{1}{r^2} (hx^T + xh^T) - \frac{2x^T h}{r^4} x x^T \right), \\ \nabla^2 \kappa(x)[h, k] &= \frac{1}{4\pi} \left(-\frac{k^T h}{r^2} I_2 + \frac{2(x^T h)(x^T k)}{r^4} I_2 + \frac{1}{r^2} (hk^T + kh^T) \right. \\ &\quad \left. - \frac{2x^T k}{r^4} (hx^T + xh^T) - \frac{2x^T h}{r^4} (kx^T + xk^T) - \frac{2k^T h}{r^4} x x^T + \frac{8(x^T h)(x^T k)}{r^6} x x^T \right). \end{aligned}$$

Thus, for $0 < r \leq 1$, we have $\|\kappa(x)\|_2 \leq r^{-1}$, $\|\nabla \kappa(x)\|_2 \lesssim r^{-1} \leq r^{-2}$ and $\|\nabla^2 \kappa(x)\|_2 \lesssim r^{-2} \leq r^{-3}$.

- For the 3D Laplacian single layer kernel, $\kappa(x) = (4\pi)^{-1}/r$, we have

$$\nabla \kappa(x) = -(4\pi)^{-1} x/r^3, \quad \nabla^2 \kappa(x) = -(4\pi)^{-1} \left(\frac{1}{r^3} I_3 - \frac{3}{r^5} x x^T \right).$$

Hence, for $0 < r \leq 1$, we have $|\kappa(x)| \lesssim r^{-1} \leq r^{-2}$, $\|\nabla \kappa(x)\|_2 \lesssim r^{-2} \leq r^{-3}$, and $\|\nabla^2 \kappa(x)\|_2 \lesssim r^{-3} \leq r^{-4}$.

- For the 3D modified Laplacian double layer kernel, $\kappa(x) = -(4\pi)^{-1} x/r^3$, we have

$$\begin{aligned} \nabla \kappa(x) &= \frac{-1}{4\pi} \left(\frac{1}{r^3} I_3 - \frac{3}{r^5} x x^T \right), \\ \nabla^2 \kappa(x)[h] &= \frac{-1}{4\pi} \left(\frac{15x^T h}{r^7} x x^T - \frac{3}{r^5} (xh^T + hx^T + x^T h I_3) \right). \end{aligned}$$

Thus, for $0 < r \leq 1$, $\|\kappa(x)\|_2 \lesssim r^{-2}$, $\|\nabla \kappa(x)\|_2 \lesssim r^{-3}$, and $\|\nabla^2 \kappa(x)\|_2 \lesssim r^{-4}$. As above, the Laplacian double layer and adjoint double layer kernels obtained by multiplying by bounded unit normals have the same singular order and satisfy the same bounds.

- For the 3D Stokeslet, $\kappa(x) = \frac{1}{8\pi} \left(\frac{1}{r} I_3 + \frac{x x^T}{r^3} \right)$, we have

$$\begin{aligned} \nabla \kappa(x)[h] &= \frac{1}{8\pi} \left(-\frac{x^T h}{r^3} I_3 + \frac{1}{r^3} (hx^T + xh^T) - \frac{3x^T h}{r^5} x x^T \right), \\ \nabla^2 \kappa(x)[h, k] &= \frac{1}{8\pi} \left(-\frac{k^T h}{r^3} I_3 + \frac{3(x^T h)(x^T k)}{r^5} I_3 + \frac{1}{r^3} (hk^T + kh^T) \right. \\ &\quad \left. - \frac{3x^T k}{r^5} (hx^T + xh^T) - \frac{3x^T h}{r^5} (kx^T + xk^T) - \frac{3k^T h}{r^5} x x^T + \frac{15(x^T h)(x^T k)}{r^7} x x^T \right). \end{aligned}$$

Therefore, for $0 < r \leq 1$, $\|\kappa(x)\|_2 \lesssim r^{-1} \leq r^{-2}$, $\|\nabla \kappa(x)\|_2 \lesssim r^{-2} \leq r^{-3}$ and $\|\nabla^2 \kappa(x)\|_2 \lesssim r^{-3} \leq r^{-4}$.

B.2. Short-Range Asymptotic Approximation. We now derive short-range asymptotic approximations for the kernel integrals

$$(B.3) \quad \int_{\partial\Omega \cap B_\epsilon(x)} \kappa'(x - y, n_x, n_y) f(y) dy.$$

Fix a target point x . We introduce a local coordinate system by mapping y to

$$(B.4) \quad \tilde{y} = Q(y - x),$$

so that x is mapped to the origin and the tangent and normal directions at x form the coordinate axes.

We first consider the two-dimensional case. Let τ_x and n_x denote the tangent and outward unit normal at x (right-hand convention). Define the orthogonal transformation matrix by $Q^T = [\tau_x \ n_x]$. In the local coordinate, the boundary segment $\partial\Omega \cap B_\epsilon(x)$ can be parameterized as $\tilde{y}(s) = (s, h(s))$, $s \in [-\epsilon, \epsilon]$, where $h(0) = 0$ and $h'(0) = 0$. The outward unit normal and the surface measure are given by $\tilde{n}_{\tilde{y}} = \frac{(h'(s), -1)}{\sqrt{1+h'(s)^2}}$ and $d\tilde{y} = \sqrt{1+h'(s)^2} ds$. Applying Taylor expansions about $s = 0$, we have

$$(B.5) \quad \begin{aligned} h(s) &= \frac{h''(0)}{2}s^2 + \frac{h^{(3)}(0)}{6}s^3 + \mathcal{O}(s^4), \\ \frac{1}{s^2 + h(s)^2} &= \frac{1}{s^2(1 + \frac{h''(0)^2}{4}s^2 + \mathcal{O}(s^3))} = \frac{1}{s^2} - \frac{h''(0)^2}{4} + \mathcal{O}(s), \\ \sqrt{1 + h'(s)^2} &= 1 + \frac{h''(0)^2}{2}s^2 + \mathcal{O}(s^3), \\ f(y) &= \tilde{f}((s, h(s))) = f(x) + \nabla f(x) \cdot \tau_x s + \mathcal{O}(s^2). \end{aligned}$$

The tangential (curve) gradient of the outward normal satisfies

$$(B.6) \quad \nabla_{\mathcal{D}} n_y \Big|_{y=x} = Q^T \nabla_{\tilde{\mathcal{D}}} \tilde{n}_{\tilde{y}} \Big|_{\tilde{y}=\tilde{x}} Q = Q^T \begin{bmatrix} h''(0) & 0 \\ 0 & 0 \end{bmatrix} Q.$$

Here, $\nabla_{\mathcal{D}}$ denotes the tangential (curve) gradient. Locally at x , it reduces to $\nabla_{\mathcal{D}}|_x = (I - n_x \otimes n_x) \nabla = \tau_x \partial_s$. From (B.6), we therefore identify $h''(0) = \text{tr}[\nabla_{\mathcal{D}} n_y \Big|_{y=x}]$. Using these expansions in (B.5), we derive the leading-order contributions of the short-range integrals for each kernel, summarized below.

- For the 2D Laplace single layer potential, we have

$$\begin{aligned} \int_{\partial\Omega \cap B_\epsilon(x)} \frac{-1}{2\pi} \log \|x - y\|_2 f(y) dy &= \frac{-1}{4\pi} \int_{-\epsilon}^{\epsilon} \log(s^2 + h(s)^2) \tilde{f}((s, h(s))) \sqrt{1 + h'(s)^2} ds \\ &= -\frac{1}{\pi} f(x) (\epsilon \log \epsilon - \epsilon) + o(\epsilon^2). \end{aligned}$$

- For the 2D Laplace double layer potential, we have

$$\begin{aligned} \int_{\partial\Omega \cap B_\epsilon(x)} \frac{(x - y) \cdot n_y}{2\pi \|x - y\|_2^2} f(y) dy &= \int_{-\epsilon}^{\epsilon} \frac{(-s, -h(s)) \cdot (h'(s), -1)}{2\pi(s^2 + h(s)^2)} \tilde{f}((s, h(s))) ds \\ &= -\frac{h''(0)}{2\pi} f(x) \epsilon + \mathcal{O}(\epsilon^3). \end{aligned}$$

- For the 2D modified Laplace double layer potential, we have

$$\begin{aligned}
\int_{\partial\Omega \cap B_\epsilon(x)} \frac{x-y}{2\pi\|x-y\|_2^2} f(y) dy &= Q^T \int_{-\epsilon}^{\epsilon} \frac{(-s, -h(s))}{2\pi(s^2 + h(s)^2)} \sqrt{1+h'(s)^2} \tilde{f}((s, h(s))) ds \\
&= -\frac{\epsilon}{2\pi} Q^T \begin{bmatrix} 2\nabla f(x) \cdot \tau_x \\ h''(0)f(x) \end{bmatrix} + \mathcal{O}(\epsilon^2) \\
&= -\frac{\epsilon}{2\pi} \left(2\nabla_D f(x) + h''(0)f(x)n_x \right) + \mathcal{O}(\epsilon^3).
\end{aligned}$$

- For the 2D adjoint Laplace double layer potential, applying the same local approximation as for the modified Laplace double layer potential yields

$$\int_{\partial\Omega \cap B_\epsilon(x)} \frac{(y-x) \cdot n_x}{2\pi\|x-y\|_2^2} f(y) dy = -\frac{h''(0)}{2\pi} f(x)\epsilon + \mathcal{O}(\epsilon^3).$$

- For the 2D Stokeslet, we have

$$\begin{aligned}
&\int_{\partial\Omega \cap B_\epsilon(x)} \frac{1}{4\pi} \left(-\log\|x-y\|_2 I_2 + \frac{(x-y)(x-y)^T}{\|x-y\|_2^2} \right) f(y) ds \\
&= \frac{-1}{2\pi} (\epsilon \log \epsilon - \epsilon) f(x) + o(\epsilon^2) + \int_{-\epsilon}^{\epsilon} Q^T \frac{1}{4\pi} \left(\frac{1}{s^2 + h(s)^2} \begin{bmatrix} s^2 & sh(s) \\ sh(s) & h(s)^2 \end{bmatrix} \right) Q \tilde{f}((s, h(s))) \sqrt{1+h'(s)^2} ds \\
&= \frac{-1}{2\pi} (\epsilon \log \epsilon - \epsilon) f(x) + \frac{1}{2\pi} Q^T \begin{bmatrix} 1 & 0 \\ 0 & 0 \end{bmatrix} Q f(x) \epsilon + o(\epsilon^2) \\
&= \frac{-1}{2\pi} (\epsilon \log \epsilon - \epsilon) f(x) + \frac{1}{2\pi} (I_2 - n_x n_x^T) f(x) \epsilon + o(\epsilon^2).
\end{aligned}$$

We then consider the three-dimensional case. Let $\tau_{x,1}$, $\tau_{x,2}$, and n_x denote two orthonormal tangent directions and the outward unit normal at x , respectively. Define the orthogonal transformation matrix Q in (B.4) by $Q^T = [\tau_{x,1} \ \tau_{x,2} \ n_x]$. In the local coordinate, the local surface patch $\partial\Omega \cap B_\epsilon(x)$ can be parameterized as $\tilde{y}(s) = (s, h(s))$, $s = (s_1, s_2) \in B_\epsilon(0)$ where $h((0,0)) = 0$ and $\nabla h((0,0)) = 0$. The outward unit normal is $\tilde{n}_{\tilde{y}} = \frac{(\partial_1 h(s), \partial_2 h(s), -1)}{\sqrt{1+\partial_1 h(s)^2 + \partial_2 h(s)^2}}$ and the surface measure satisfies $d\tilde{y} = \sqrt{1+\partial_1 h(s)^2 + \partial_2 h(s)^2} ds$. Applying Taylor expansions about $s = (0,0)$, we have

$$\begin{aligned}
(B.7) \quad h(s) &= \frac{1}{2} s^T \nabla^2 h(0) s + \mathcal{O}(s^3), \\
(s^T s + h(s)^2)^{-3/2} &= \frac{1}{(s^T s)^{3/2}} \left(1 - \frac{3}{8} \frac{(s^T \nabla^2 h(0) s)^2}{s^T s} \right) + \mathcal{O}(1), \\
(s^T s + h(s)^2)^{-1/2} &= \frac{1}{(s^T s)^{1/2}} \left(1 - \frac{1}{8} \frac{(s^T \nabla^2 h(0) s)^2}{s^T s} \right) + \mathcal{O}(\|s\|_2^2), \\
\sqrt{1+\partial_1 h(s)^2 + \partial_2 h(s)^2} &= 1 + \frac{1}{2} s^T \nabla^2 h(0) \nabla^2 h(0) s + \mathcal{O}(\|s\|_2^3), \\
f(y) &= \tilde{f}((s, h(s))) = f(x) + \sum_{i=1}^2 \nabla f(x) \cdot \tau_{x,i} s_i + \mathcal{O}(\|s\|_2^2).
\end{aligned}$$

The tangential (surface) gradient of the outward normal satisfies

$$(B.8) \quad \nabla_{\mathcal{D}} n_y|_{y=x} = Q^T \nabla_{\tilde{\mathcal{D}}} \tilde{n}_{\tilde{y}}|_{\tilde{y}=\tilde{x}} Q = Q^T \begin{bmatrix} \partial_{11} h(0) & \partial_{12} h(0) & 0 \\ \partial_{21} h(0) & \partial_{22} h(0) & 0 \\ 0 & 0 & 0 \end{bmatrix} Q.$$

Here $\nabla_{\mathcal{D}}$ denotes the tangential (surface) gradient. Locally, $\nabla_{\mathcal{D}}|_x = (I - n_x \otimes n_x) \nabla = \sum_{i=1}^2 \tau_{x,i} \partial_{s_i}$. Consequently, $\Delta h(0) = \text{tr}[\nabla_{\mathcal{D}} n_y|_{y=x}]$. Using these expansions in (B.7), we now derive the leading-order contributions of the short-range integrals for each kernel.

- For the 3D Laplace single layer potential, we have

$$\begin{aligned} \int_{\partial\Omega \cap B_\epsilon(x)} \frac{1}{4\pi \|x-y\|_2} f(y) dy &= \frac{1}{4\pi} \int_{B_\epsilon(0)} (s^T s + h(s)^2)^{-1/2} \sqrt{1 + \partial_1 h(s)^2 + \partial_2 h(s)^2} \tilde{f}((s, h(s))) ds \\ &= \frac{1}{4\pi} \int_{B_\epsilon(0)} \left(\frac{1}{(s^T s)^{1/2}} + \mathcal{O}(\|s\|_2) \right) (f(x) + \sum_{i=1,2} \nabla f(x) \cdot \tau_{x,i} s_i + \mathcal{O}(\|s\|_2^2)) ds \\ &= \frac{\epsilon}{2} f(x) + \mathcal{O}(\epsilon^3). \end{aligned}$$

- For the 3D Laplace double layer potential, we have

$$\begin{aligned} \int_{\partial\Omega \cap B_\epsilon(x)} \frac{(y-x) \cdot n_y}{4\pi \|x-y\|_2^3} f(y) dy &= \frac{1}{4\pi} \int_{B_\epsilon(0)} \frac{s^T \nabla h(s) - h(s)}{(s^T s + h(s)^2)^{3/2}} (f(x) + \sum_{i=1}^2 \nabla f(x) \cdot \tau_{x,i} s_i + \mathcal{O}(\|s\|_2^2)) ds \\ &= \frac{1}{4\pi} \int_{B_\epsilon(0)} \frac{1}{(s^T s)^{3/2}} \left(1 - \frac{3}{8} \frac{(s^T \nabla^2 h(0) s)^2}{s^T s} \right) \frac{1}{2} s^T \nabla^2 h(0) s ds + \mathcal{O}(\epsilon^3) \\ &= \frac{1}{4\pi} \int_{B_\epsilon(0)} \frac{s^T \nabla^2 h(0) s}{2(s^T s)^{3/2}} ds + \mathcal{O}(\epsilon^3) \\ &= \frac{\epsilon}{8} \Delta h(0) f(x) + \mathcal{O}(\epsilon^3). \end{aligned}$$

- For the 3D modified Laplace double layer potential, we have

$$\begin{aligned} \int_{\partial\Omega \cap B_\epsilon(x)} \frac{y-x}{4\pi \|x-y\|_2^3} f(y) dy &= Q^T \int_{B_\epsilon(0)} \frac{(s, h(s))}{4\pi (s^T s + h(s)^2)^{3/2}} \sqrt{1 + \partial_1 h(s)^2 + \partial_2 h(s)^2} \tilde{f}((s, h(s))) ds \\ &= Q^T \int_{B_\epsilon(0)} \frac{(s, \frac{1}{2} s^T \nabla^2 h(0) s)}{4\pi (s^T s)^{3/2}} (f(x) + \sum_{i=1}^2 \nabla f(x) \cdot \tau_{x,i} s_i) ds + \mathcal{O}(\epsilon^3) \\ &= \frac{\epsilon}{8} Q^T \begin{bmatrix} \nabla f(x) \cdot \tau_{x,1} \\ \nabla f(x) \cdot \tau_{x,2} \\ \Delta h(0) f(x) \end{bmatrix} + \mathcal{O}(\epsilon^3) \\ &= \frac{\epsilon}{8} \left(2 \nabla_{\mathcal{D}} f(x) + \Delta h(0) f(x) n_x \right) + \mathcal{O}(\epsilon^3). \end{aligned}$$

- For the 3D adjoint Laplace double layer potential, applying the same local approximation as for the modified Laplace double layer potential yields

$$\int_{\partial\Omega \cap B_\epsilon(x)} \frac{(x-y) \cdot n_x}{4\pi \|x-y\|_2^2} f(y) dy = \frac{\epsilon}{8} \Delta h(0) f(x) + \mathcal{O}(\epsilon^3).$$

- For the 3D Stokeslet, we have

$$\begin{aligned}
& \int_{\partial\Omega \cap B_\epsilon(x)} \frac{1}{8\pi} \left(\frac{1}{\|x-y\|_2} I_3 + \frac{(x-y)(x-y)^T}{\|x-y\|_2^3} \right) f(y) ds(y) \\
&= \frac{\epsilon}{4} f(x) + \frac{1}{8\pi} \int_{B_\epsilon(0)} Q^T \left((s^T s + h^2(s))^{-3/2} \begin{bmatrix} ss^T & h(s)s \\ h(s)s^T & h(s)^2 \end{bmatrix} \right) Q \left(f(x) + \sum_{i=1}^2 \nabla f(x) \cdot \tau_{x,i} s_i \right) ds + \mathcal{O}(\epsilon^3) \\
&= \frac{\epsilon}{4} f(x) + \frac{1}{8\pi} \int_{B_\epsilon(0)} Q^T (s^T s)^{-3/2} \left(\begin{bmatrix} ss^T & 0 \\ 0 & 0 \end{bmatrix} Q \left(f(x) + \sum_{i=1}^2 (\nabla f(x) \cdot \tau_{x,i}) s_i \right) \right) ds + \mathcal{O}(\epsilon^3) \\
&= \frac{\epsilon}{4} f(x) + \frac{1}{8\pi} \int_{B_\epsilon(0)} Q^T (s^T s)^{-3/2} \left(\begin{bmatrix} ss^T & 0 \\ 0 & 0 \end{bmatrix} Q f(x) \right) ds + \mathcal{O}(\epsilon^3) \\
&= \frac{\epsilon}{4} f(x) + \frac{1}{8\pi} Q^T \begin{bmatrix} \epsilon\pi I_2 & 0 \\ 0 & 0 \end{bmatrix} Q f(x) + \mathcal{O}(\epsilon^3) \\
&= \frac{\epsilon}{4} f(x) + \frac{\epsilon}{8} (I_3 - n_x n_x^T) f(x) + \mathcal{O}(\epsilon^3).
\end{aligned}$$

B.3. Numerical Evaluation of Kernel Integrals. We conclude by describing the numerical evaluation of the 2D kernel integrals

$$u(x) = \int_{\partial\Omega} \kappa(x-y; n_x, n_y) f(y) dy,$$

introduced in [subsection 5.1](#), using a panel method. We discretize the curve $\partial\Omega$ into N panels, $\partial\Omega = \cup_{i=1}^N \Gamma_i$, ordered counterclockwise. On each panel, both the density f and the solution u are approximated by piecewise constant functions. For a given panel Γ of length l and orientation angle θ , let $\tau = [\cos \theta, \sin \theta]^T$ and $n = [\sin \theta, -\cos \theta]^T$ denote the unit tangent and outward unit normal of the panel, respectively. We introduce a local reference coordinate system via the transformation

$$(B.9) \quad \tilde{x} = Q(x-b), \quad Q^T = \begin{bmatrix} \cos \theta & -\sin \theta \\ \sin \theta & \cos \theta \end{bmatrix} = [\tau \ n],$$

where b is the starting point of the panel, which is mapped to the origin, and the panel is aligned with the \tilde{x}_1 -axis. Writing $\tilde{x} = (\tilde{x}_1, \tilde{x}_2)$, the panel integrals are evaluated in this local reference frame and then transformed back to the global coordinates. Closed-form expressions for each kernel integral on Γ are listed below:

- For the 2D Laplacian single layer potential, if $\tilde{x}_2 \neq 0$, then

$$\begin{aligned}
\int_{\Gamma} \kappa(x-y) dy &= -\frac{1}{2\pi} \left((l-\tilde{x}_1) \ln \sqrt{(l-\tilde{x}_1)^2 + \tilde{x}_2^2} + \tilde{x}_1 \ln \sqrt{\tilde{x}_1^2 + \tilde{x}_2^2} - l \right. \\
&\quad \left. + \tilde{x}_2 \arctan\left(\frac{l-\tilde{x}_1}{\tilde{x}_2}\right) + \tilde{x}_2 \arctan\left(\frac{\tilde{x}_1}{\tilde{x}_2}\right) \right).
\end{aligned}$$

If $\tilde{x}_2 = 0$, then

$$\int_{\Gamma} \kappa(x-y) dy = -\frac{1}{2\pi} \left((l-\tilde{x}_1) \ln \sqrt{(l-\tilde{x}_1)^2} + \tilde{x}_1 \ln \sqrt{\tilde{x}_1^2} - l \right).$$

- For the 2D Laplacian double layer potential, since the panels are ordered counterclockwise, in the local coordinates [\(B.9\)](#), the outward unit normal is $\tilde{n}_{\tilde{y}} = (0, -1)$. If $\tilde{x}_2 \neq 0$, then

$$\int_{\Gamma} \kappa(x-y, n_y) dy = -\frac{1}{2\pi} \left[\arctan\left(\frac{\tilde{x}_1}{\tilde{x}_2}\right) + \arctan\left(\frac{l-\tilde{x}_1}{\tilde{x}_2}\right) \right].$$

If $\tilde{x}_2 = 0$, the integral vanishes:

$$\int_{\Gamma} \kappa(x - y, n_y) dy = 0.$$

- For the 2D modified Laplacian double layer potential, if $\tilde{x}_2 \neq 0$, then

$$\int_{\Gamma} \kappa(x - y) dy = \frac{1}{2\pi} \left[\ln \sqrt{\frac{\tilde{x}_1^2 + \tilde{x}_2^2}{(l - \tilde{x}_1)^2 + \tilde{x}_2^2}}, \arctan\left(\frac{\tilde{x}_1}{\tilde{x}_2}\right) + \arctan\left(\frac{l - \tilde{x}_1}{\tilde{x}_2}\right) \right] Q.$$

If $\tilde{x}_2 = 0$, the integral is interpreted in the Cauchy principal value sense and reduces to

$$\int_{\Gamma} \kappa(x - y) dy = \frac{1}{2\pi} \left[\ln \sqrt{\frac{\tilde{x}_1^2}{(l - \tilde{x}_1)^2}}, 0 \right] Q.$$

- For the 2D adjoint Laplacian double layer potential, if $\tilde{x}_2 \neq 0$, then

$$\int_{\Gamma} \kappa(x - y, n_x) dy = -\frac{1}{2\pi} \left[\ln \sqrt{\frac{\tilde{x}_1^2 + \tilde{x}_2^2}{(l - \tilde{x}_1)^2 + \tilde{x}_2^2}}, \arctan\left(\frac{\tilde{x}_1}{\tilde{x}_2}\right) + \arctan\left(\frac{l - \tilde{x}_1}{\tilde{x}_2}\right) \right] Q n_x.$$

If $\tilde{x}_2 = 0$, then

$$\int_{\Gamma} \kappa(x - y, n_x) dy = \frac{1}{2\pi} \left[\ln \sqrt{\frac{\tilde{x}_1^2}{(l - \tilde{x}_1)^2}}, 0 \right] Q n_x.$$

- For the 2D Stokeslet, if $\tilde{x}_2 \neq 0$, then

$$\int_{\Gamma} \frac{(x - y)(x - y)^T}{\|x - y\|_2^2} dy = Q^T \begin{bmatrix} l - x_2 \left(\arctan\left(\frac{\tilde{x}_1}{\tilde{x}_2}\right) + \arctan\left(\frac{l - \tilde{x}_1}{\tilde{x}_2}\right) \right) & \tilde{x}_2 \ln \sqrt{\frac{\tilde{x}_1^2 + \tilde{x}_2^2}{(l - \tilde{x}_1)^2 + \tilde{x}_2^2}} \\ * & \tilde{x}_2 \left(\arctan\left(\frac{\tilde{x}_1}{\tilde{x}_2}\right) + \arctan\left(\frac{l - \tilde{x}_1}{\tilde{x}_2}\right) \right) \end{bmatrix} Q.$$

If $\tilde{x}_2 = 0$, then

$$\int_{\Gamma} \frac{(x - y)(x - y)^T}{\|x - y\|_2^2} dy = Q^T \begin{bmatrix} l & 0 \\ 0 & 0 \end{bmatrix} Q.$$

REFERENCES

- [1] D. AMSALLEM, M. ZAHR, Y. CHOI, AND C. FARHAT, *Design optimization using hyper-reduced-order models*, Structural and Multidisciplinary Optimization, 51 (2015), pp. 919–940.
- [2] C. R. ANDERSON, *An implementation of the fast multipole method without multipoles*, SIAM Journal on Scientific and Statistical Computing, 13 (1992), pp. 923–947.
- [3] J. BARNES AND P. HUT, *A hierarchical $o(n \log n)$ force-calculation algorithm*, nature, 324 (1986), pp. 446–449.
- [4] M. BEBENDORF, *Approximation of boundary element matrices*, Numerische Mathematik, 86 (2000), pp. 565–589.
- [5] E. BLESZYNSKI, M. BLESZYNSKI, AND T. JAROSZEWICZ, *Aim: Adaptive integral method for solving large-scale electromagnetic scattering and radiation problems*, Radio Science, 31 (1996), pp. 1225–1251.
- [6] S. BÖRM, L. GRASEDYCK, AND W. HACKBUSCH, *Introduction to hierarchical matrices with applications*, Engineering analysis with boundary elements, 27 (2003), pp. 405–422.
- [7] N. BOULLÉ, D. HALIKIAS, AND A. TOWNSEND, *Elliptic pde learning is provably data-efficient*, Proceedings of the National Academy of Sciences, 120 (2023), p. e2303904120.

- [8] N. BOULLÉ, S. KIM, T. SHI, AND A. TOWNSEND, *Learning green's functions associated with time-dependent partial differential equations*, Journal of Machine Learning Research, 23 (2022), pp. 1–34.
- [9] O. P. BRUNO AND L. A. KUNYANSKY, *A fast, high-order algorithm for the solution of surface scattering problems: basic implementation, tests, and applications*, Journal of Computational Physics, 169 (2001), pp. 80–110.
- [10] Q. CAO, S. GOSWAMI, AND G. E. KARNIADAKIS, *Laplace neural operator for solving differential equations*, Nature Machine Intelligence, 6 (2024), pp. 631–640.
- [11] S. CAO, *Choose a transformer: Fourier or galerkin*, Advances in neural information processing systems, 34 (2021), pp. 24924–24940.
- [12] H. CHENG, L. GREENGARD, AND V. ROKHLIN, *A fast adaptive multipole algorithm in three dimensions*, Journal of computational physics, 155 (1999), pp. 468–498.
- [13] T. DARDEN, D. YORK, L. PEDERSEN, ET AL., *Particle mesh ewald: An $n \log(n)$ method for ewald sums in large systems*, Journal of chemical physics, 98 (1993), pp. 10089–10089.
- [14] M. V. DE HOOP, D. Z. HUANG, E. QIAN, AND A. M. STUART, *The cost-accuracy trade-off in operator learning with neural networks*, arXiv preprint arXiv:2203.13181, (2022).
- [15] J. DUVAL AND K. DURAISAMY, *Discretization-independent surrogate modeling of physical fields around variable geometries using coordinate-based networks*, Data-Centric Engineering, 6 (2025), p. e5.
- [16] M. ELREFAIE, F. MORAR, A. DAI, AND F. AHMED, *Drivaernet++: A large-scale multimodal car dataset with computational fluid dynamics simulations and deep learning benchmarks*, arXiv preprint arXiv:2406.09624, (2025).
- [17] P. P. EWALD, *Die berechnung optischer und elektrostatischer gitterpotentiale*, Annalen der physik, 369 (1921), pp. 253–287.
- [18] Y. FAN, J. FELIU-FABA, L. LIN, L. YING, AND L. ZEPEDA-NÚÑEZ, *A multiscale neural network based on hierarchical nested bases*, Research in the Mathematical Sciences, 6 (2019), p. 21.
- [19] Y. FAN, L. LIN, L. YING, AND L. ZEPEDA-NÚÑEZ, *A multiscale neural network based on hierarchical matrices*, Multiscale Modeling & Simulation, 17 (2019), pp. 1189–1213.
- [20] W. FONG AND E. DARVE, *The black-box fast multipole method*, Journal of Computational Physics, 228 (2009), pp. 8712–8725.
- [21] H. GAO, S. KALTENBACH, AND P. KOUMOUTSAKOS, *Generative learning of the solution of parametric partial differential equations using guided diffusion models and virtual observations*, Computer Methods in Applied Mechanics and Engineering, 435 (2025), p. 117654.
- [22] H. GAO, L. SUN, AND J.-X. WANG, *Phygeonet: Physics-informed geometry-adaptive convolutional neural networks for solving parameterized steady-state pdes on irregular domain*, Journal of Computational Physics, 428 (2021), p. 110079.
- [23] C. R. GIN, D. E. SHEA, S. L. BRUNTON, AND J. N. KUTZ, *Deepgreen: deep learning of green's functions for nonlinear boundary value problems*, Scientific reports, 11 (2021), p. 21614.
- [24] S. GOSWAMI, K. KONTOLATI, M. D. SHIELDS, AND G. E. KARNIADAKIS, *Deep transfer operator learning for partial differential equations under conditional shift*, Nature Machine Intelligence, 4 (2022), pp. 1155–1164.
- [25] L. GREENGARD AND V. ROKHLIN, *A fast algorithm for particle simulations*, Journal of computational physics, 73 (1987), pp. 325–348.
- [26] L. GREENGARD AND J. STRAIN, *A fast algorithm for the evaluation of heat potentials*, Communications on Pure and Applied Mathematics, 43 (1990), pp. 949–963.
- [27] R. GUO, J. JIANG, B. JIN, W. REN, AND J. ZHANG, *A warm-basis method for bridging learning and iteration: a case study in fluorescence molecular tomography*, arXiv preprint arXiv:2510.05926, (2025).
- [28] W. HACKBUSCH AND B. N. KHOROMSKIJ, *A sparse \mathcal{H} -matrix arithmetic. part ii: Application to multi-dimensional problems*, Computing, 64 (2000), pp. 21–47.
- [29] J. HE, S. KORIC, D. ABUEIDDA, A. NAJAFI, AND I. JASIUK, *Geom-deeponet: A point-cloud-based deep operator network for field predictions on 3d parameterized geometries*, Computer Methods in Applied Mechanics and Engineering, 429 (2024), p. 117130.
- [30] K. HE, X. ZHANG, S. REN, AND J. SUN, *Deep residual learning for image recognition*, in Proceedings of the IEEE conference on computer vision and pattern recognition, 2016, pp. 770–778.
- [31] D. HENDRYCKS AND K. GIMPEL, *Gaussian error linear units (gelus)*, arXiv preprint arXiv:1606.08415, (2016).
- [32] J. HESS AND A. SMITH, *Calculation of potential flow about arbitrary bodies*, Progress in aeronautical sciences, 8 (1967), pp. 1–138.
- [33] R. W. HOCKNEY AND J. W. EASTWOOD, *Computer simulation using particles*, crc Press, 2021.
- [34] J. HU, P. JIN, AND W. ZHANG, *Manifold function encoder: Identifying different functions*

defined on different manifolds, arXiv preprint arXiv:2512.20227, (2025).

[35] D. Z. HUANG, N. H. NELSEN, AND M. TRAUTNER, *An operator learning perspective on parameter-to-observable maps*, arXiv preprint arXiv:2402.06031, (2024).

[36] C. JUNFENG AND K. WU, *Positional knowledge is all you need: Position-induced transformer (pit) for operator learning*, in Forty-first International Conference on Machine Learning, 2024.

[37] Y. KHOO AND L. YING, *Switchnet: a neural network model for forward and inverse scattering problems*, SIAM Journal on Scientific Computing, 41 (2019), pp. A3182–A3201.

[38] D. P. KINGMA AND J. BA, *Adam: A method for stochastic optimization*, International Conference on Learning Representations, (2015), <https://arxiv.org/abs/1412.6980>.

[39] B. O. KOOPMAN, *Hamiltonian systems and transformation in hilbert space*, Proceedings of the National Academy of Sciences, 17 (1931), pp. 315–318.

[40] N. KOVACHKI, Z. LI, B. LIU, K. AZIZZADENESHELI, K. BHATTACHARYA, A. STUART, AND A. ANANDKUMAR, *Neural operator: Learning maps between function spaces with applications to pdes*, Journal of Machine Learning Research, 24 (2023), pp. 1–97.

[41] R. KRESS, *Linear integral equations*, vol. 82, Springer, 1989.

[42] J. LI, X. DU, AND J. R. MARTINS, *Machine learning in aerodynamic shape optimization*, Progress in Aerospace Sciences, 134 (2022), p. 100849.

[43] Y. LI, R. BU, M. SUN, W. WU, X. DI, AND B. CHEN, *Pointcnn: Convolution on x-transformed points*, Advances in neural information processing systems, 31 (2018).

[44] Z. LI, D. Z. HUANG, B. LIU, AND A. ANANDKUMAR, *Fourier neural operator with learned deformations for pdes on general geometries*, Journal of Machine Learning Research, 24 (2023), pp. 1–26.

[45] Z. LI, N. KOVACHKI, K. AZIZZADENESHELI, B. LIU, K. BHATTACHARYA, A. STUART, AND A. ANANDKUMAR, *Fourier neural operator for parametric partial differential equations*, arXiv preprint arXiv:2010.08895, (2020).

[46] Z. LI, N. KOVACHKI, K. AZIZZADENESHELI, B. LIU, K. BHATTACHARYA, A. STUART, AND A. ANANDKUMAR, *Neural operator: Graph kernel network for partial differential equations*, arXiv preprint arXiv:2003.03485, (2020).

[47] Z. LI, N. KOVACHKI, K. AZIZZADENESHELI, B. LIU, A. STUART, K. BHATTACHARYA, AND A. ANANDKUMAR, *Multipole graph neural operator for parametric partial differential equations*, Advances in Neural Information Processing Systems, 33 (2020), pp. 6755–6766.

[48] Z. LI, N. KOVACHKI, C. CHOY, B. LI, J. KOSSAIFI, S. OTTA, M. A. NABIAN, M. STADLER, C. HUNDT, K. AZIZZADENESHELI, ET AL., *Geometry-informed neural operator for large-scale 3d pdes*, Advances in Neural Information Processing Systems, 36 (2024).

[49] L. LINGSCH, M. Y. MICHELIS, E. DE BEZENAC, S. M. PERERA, R. K. KATZSCHMANN, AND S. MISHRA, *Beyond regular grids: Fourier-based neural operators on arbitrary domains*, arXiv preprint arXiv:2305.19663, (2023).

[50] N. LIU, S. JAFARZADEH, AND Y. YU, *Domain agnostic fourier neural operators*, Advances in Neural Information Processing Systems, 36 (2024).

[51] X. LIU, H. LIN, X. LIU, J. QIAN, S. CAI, H. FAN, AND Q. GAO, *Laflownet: A dynamic graph method for the prediction of velocity and pressure fields in left atrium and left atrial appendage*, Engineering Applications of Artificial Intelligence, 136 (2024), p. 108896.

[52] M. LIU-SCHIAFFINI, J. BERNER, B. BONEV, T. KURTH, K. AZIZZADENESHELI, AND A. ANANDKUMAR, *Neural operators with localized integral and differential kernels*, arXiv preprint arXiv:2402.16845, (2024).

[53] L. LU, P. JIN, G. PANG, Z. ZHANG, AND G. E. KARNIADAKIS, *Learning nonlinear operators via deeponet based on the universal approximation theorem of operators*, Nature machine intelligence, 3 (2021), pp. 218–229.

[54] D. LUO, T. O'LEARY-ROSEBERRY, P. CHEN, AND O. GHATTAS, *Efficient pde-constrained optimization under high-dimensional uncertainty using derivative-informed neural operators*, SIAM Journal on Scientific Computing, 47 (2025), pp. C899–C931.

[55] I. MEZIĆ, *Spectral properties of dynamical systems, model reduction and decompositions*, Nonlinear Dynamics, 41 (2005), pp. 309–325.

[56] S. MOUSAVI, S. WEN, L. LINGSCH, M. HERDE, B. RAONIĆ, AND S. MISHRA, *Rigno: A graph-based framework for robust and accurate operator learning for pdes on arbitrary domains*, arXiv preprint arXiv:2501.19205, (2025).

[57] N. H. NELSEN AND A. M. STUART, *The random feature model for input-output maps between banach spaces*, SIAM Journal on Scientific Computing, 43 (2021), pp. A3212–A3243.

[58] T. PFAFF, M. FORTUNATO, A. SANCHEZ-GONZALEZ, AND P. W. BATTAGLIA, *Learning mesh-based simulation with graph networks*, arXiv preprint arXiv:2010.03409, (2020).

[59] J. R. PHILLIPS AND J. K. WHITE, *A precorrected-fft method for electrostatic analysis of com-*

pllicated 3-d structures, IEEE Transactions on computer-aided design of integrated circuits and systems, 16 (2002), pp. 1059–1072.

[60] C. R. Qi, H. Su, K. Mo, AND L. J. GUIBAS, *Pointnet: Deep learning on point sets for 3d classification and segmentation*, in Proceedings of the IEEE conference on computer vision and pattern recognition, 2017, pp. 652–660.

[61] C. R. Qi, L. Yi, H. Su, AND L. J. GUIBAS, *Pointnet++: Deep hierarchical feature learning on point sets in a metric space*, Advances in neural information processing systems, 30 (2017).

[62] B. QUACKENBUSH AND P. J. ATZBERGER, *Transferable foundation models for geometric tasks on point cloud representations: Geometric neural operators*, arXiv preprint arXiv:2503.04649, (2025).

[63] S. A. SAUTER AND C. SCHWAB, *Boundary element methods*, in Boundary Element Methods, Springer, 2010, pp. 183–287.

[64] L. SERRANO, L. LE BOUDEC, A. KASSAÏ KOUPAÏ, T. X. WANG, Y. YIN, J.-N. VITTAUT, AND P. GALLINARI, *Operator learning with neural fields: Tackling pdes on general geometries*, Advances in Neural Information Processing Systems, 36 (2023), pp. 70581–70611.

[65] Y. SHEN AND J. J. ALONSO, *A multi-fidelity double-delta wing dataset and empirical scaling laws for gnn-based aerodynamic field surrogate*, arXiv preprint arXiv:2512.20941, (2025).

[66] Y. SHEN, J. T. NEEDELS, AND J. J. ALONSO, *Vortexnet: A graph neural network-based multi-fidelity surrogate model for field predictions*, in AIAA SciTech 2025 Forum, 2025, p. 0494.

[67] V. SINGH AND K. E. WILLCOX, *Engineering design with digital thread*, Aiaa Journal, 56 (2018), pp. 4515–4528.

[68] L. N. SMITH AND N. TOPIN, *Super-convergence: Very fast training of neural networks using large learning rates*, in Artificial intelligence and machine learning for multi-domain operations applications, vol. 11006, SPIE, 2019, pp. 369–386.

[69] O. STEINBACH, *Numerical approximation methods for elliptic boundary value problems: finite and boundary elements*, Springer, 2008.

[70] J. STRAIN, *Fast potential theory. ii. layer potentials and discrete sums*, Journal of Computational Physics, 99 (1992), pp. 251–270.

[71] Q. SUN, S. LI, B. ZHENG, L. JU, AND X. XU, *Learning singularity-encoded green's functions with application to iterative methods*, arXiv preprint arXiv:2509.11580, (2025).

[72] Q. WANG, C. WANG, M. ZHANG, J. SUN, P. YANG, S. TANG, AND S. XIANG, *Mno: Multiscale neural operator for computational fluid dynamics with 3d point cloud data*, arXiv preprint arXiv:2510.16071, (2025).

[73] S. WEN, A. KUMBHAT, L. LINGSCH, S. MOUSAVI, Y. ZHAO, P. CHANDRASHEKAR, AND S. MISHRA, *Geometry aware operator transformer as an efficient and accurate neural surrogate for pdes on arbitrary domains*, arXiv preprint arXiv:2505.18781, (2025).

[74] H. WU, H. LUO, H. WANG, J. WANG, AND M. LONG, *Transolver: A fast transformer solver for pdes on general geometries*, arXiv preprint arXiv:2402.02366, (2024).

[75] S. XIAO, P. JIN, AND Y. TANG, *Learning solution operators of pdes defined on varying domains via mionet*, arXiv preprint arXiv:2402.15097, (2024).

[76] Z. YE, X. HUANG, L. CHEN, H. LIU, Z. WANG, AND B. DONG, *Pdeformer: Towards a foundation model for one-dimensional partial differential equations*, arXiv preprint arXiv:2402.12652, (2024).

[77] M. YIN, N. CHARON, R. BRODY, L. LU, N. TRAYANOVA, AND M. MAGGIONI, *Dimon: Learning solution operators of partial differential equations on a diffeomorphic family of domains*, arXiv preprint arXiv:2402.07250, (2024).

[78] L. YING, G. BIROS, AND D. ZORIN, *A kernel-independent adaptive fast multipole algorithm in two and three dimensions*, Journal of Computational Physics, 196 (2004), pp. 591–626.

[79] C. ZENG, Y. ZHANG, J. ZHOU, Y. WANG, Z. WANG, Y. LIU, L. WU, AND D. Z. HUANG, *Point cloud neural operator for parametric pdes on complex and variable geometries*, Computer Methods in Applied Mechanics and Engineering, 443 (2025), p. 118022.

[80] T. ZHOU, X. WAN, D. Z. HUANG, Z. LI, Z. PENG, A. ANANDKUMAR, J. F. BRADY, P. W. STERNBERG, AND C. DARAIO, *Ai-aided geometric design of anti-infection catheters*, Science Advances, 10 (2024), p. eadj1741.

[81] Y. ZHU AND N. ZABARAS, *Bayesian deep convolutional encoder–decoder networks for surrogate modeling and uncertainty quantification*, Journal of Computational Physics, 366 (2018), pp. 415–447.